Structural and mechanistic insights into human choline transport

Tsai-Hsuan Weng[1], Ainara Claveras Cabezudo[2,3], Wiebke Jösting[1], Andre Bazzone[4], Sonja Welsch[5], Gonca Gursu[1], Gerhard Hummer[2,6], Di Wu[1*], Schara Safarian[1,7,8*]

Affiliations

[1] *Department of Molecular Membrane Biology, Max Planck Institute of Biophysics, D-60438 Frankfurt/Main, Germany*

[2] *Department of Theoretical Biophysics, Max Planck Institute of Biophysics, D-60438 Frankfurt/Main, Germany*

[3] *IMPRS on Cellular Biophysics, D-60438 Frankfurt/Main, Germany*

[4] *Nanion Technologies GmbH, Ganghoferstr. 70a, 80339, Munich, Germany*

[5] *Central Electron Microscopy Facility, Max Planck Institute of Biophysics, D-60438 Frankfurt am Main, Germany*

[6] *Institute of Biophysics, Goethe University Frankfurt, D-60438 Frankfurt/Main, Germany*

[7] *Department of Microbiology and Immunology, School of Biomedical Sciences, University of Otago, Dunedin, NZ-9054, New Zealand*

[8] *present address: Fraunhofer Institute for Translational Medicine and Pharmacology ITMP Frankfurt, D-60438 Frankfurt/Main, Germany*

[*]Correspondence and requests for materials should be addressed to Di Wu (di.wu@biophys.mpg.de) and Schara Safarian (schara.safarian@biophys.mpg.de).

Abstract

Human feline leukaemia virus subgroup C receptor-related proteins 1 and 2 (FLVCR1 and 2) are major facilitator superfamily transporters from the solute carrier family 49. Dysregulation of these ubiquitous transporters has been linked to various haematological and neurological disorders. While both FLVCRs were initially proposed to hold a physiological function in heme transport, subsequent studies questioned this notion. Here, we used structural, computational and biochemical methods and conclude that these two FLVCRs function as human choline transporters. We present cryo-electron microscopy structures of FLVCRs in different inward- and outward-facing conformations, captured in the apo state or in complex with choline in their translocation pathways. Our findings provide insights into the molecular framework of choline coordination and transport, largely mediated by conserved cation-π interactions, and further illuminate the conformational dynamics of the transport cycle. Moreover, we identified a heme binding site on the protein surface of the FLVCR2 N-domain, and observed that heme actively drives the conformational transitions of the protein. This auxiliary binding site might indicate a potential regulatory role of heme in the FLVCR2 transport mechanisms. Our work

resolves the contested substrate specificity of the FLVCRs, and sheds light on the process of maintaining cellular choline homeostasis at the molecular level.

42 **Introduction**

43 The feline leukaemia virus subgroup C receptor (FLVCR) family, a member of the major facilitator
44 superfamily (MFS) of secondary active transporters, consists of four paralogues encoded by the human
45 *SLC49* gene group[1]. FLVCR1 (SLC49A1) was initially identified as the cell receptor for feline leukaemia
46 virus (FeLV), a retrovirus that causes profound anaemia in cats by interfering with erythropoiesis[2].
47 FLVCR2 (SLC49A2), another major member of the family, shares 60% sequence identity with FLVCR1 in
48 the transmembrane domain but does not bind to the feline leukaemia virus subgroup C envelope
49 protein[3]. Both transporters exhibit ubiquitous tissue distribution in humans and have significant
50 haemato- and neuropathological implications[1,4]. Dysfunction of FLVCR1 caused by germline mutations
51 is associated with posterior column ataxia with retinitis pigmentosa (PCARP)[5], while its alternatively
52 spliced isoforms have been linked to Diamond-Blackfan anaemia (DBA)[6]. Similarly, truncation and
53 missense mutations in the gene encoding for FLVCR2 are associated with the autosomal-recessive
54 cerebral proliferative vasculopathy known as Fowler syndrome[7,8]. Furthermore, both FLVCR variants
55 are suggested to play a key role in cell development and differentiation, including angiogenesis and
56 tumorigenesis[9–12].

57

58 Here, we studied the molecular architecture, the conformational landscape, and the contested
59 substrate specificity of human FLVCR1 and FLVCR2 using single-particle analysis cryogenic electron
60 microscopy (SPA cryo-EM) and molecular dynamics (MD) simulations. Our findings indicate that FLVCR1
61 and FLVCR2 both represent previously uncharacterized, ubiquitous human choline transporters.

62 **Results**

63 *Overall architecture of FLVCR1 and FLVCR2*

64 We stably integrated the human *SLC49A1* and *SLC49A2* genes into human embryonic kidney cells
65 (HEK293), and recombinantly produced wildtype FLVCR1a (hereafter referred to as FLVCR1) and FLVCR2
66 variants with C-terminal flag-tag modifications, respectively. Affinity-purified samples of each
67 transporter were subjected to SPA cryo-EM (Supplementary Fig. 1).

68

69 We determined the respective structures of apo FLVCR1 and FLVCR2 at 2.9 Å resolution, captured in
70 inward-facing conformations (Fig. 1a,b and Extended Data Fig. 1 and 2). Both FLVCR paralogs share a
71 common MFS-type architecture composed of 12 transmembrane α-helices (TM) arranged into two
72 pseudo-symmetrical domains[13] (Fig. 1c). In both inward-facing structures, the N-domain (TM1-6) and
73 the C-domain (TM7-12) are connected by a long and flexible loop containing two short horizontal
74 helices (H1 and H2) on the inner side of the membrane (Fig. 1). On the inner side of FLVCR2, we resolved
75 a short helical segment at the C-terminus (H3), while the density of the FLVCR1 C-terminus was less
76 pronounced (Extended Data Fig. 3). Further, we identified an N-linked glycosylation site at N265 of
77 FLVCR1 which locates within the external loop connecting TMs 5 and 6 (EL5-6; Fig. 1a). This
78 glycosylation pattern is absent in the analogous site of the FLVCR2 structure.

79

80 The inward-facing conformations of FLVCR1 and FLVCR2 exhibit a close resemblance to each other, with
81 a root mean square deviation (Cα r.m.s.d.) of 0.993 Å. Both structures feature a wedge-shaped solvent-
82 accessible cavity that is mainly created by the separation of TMs 4 and 5 of the N-domain from TMs 10
83 and 11 of the C-domain (Extended Data Fig. 4a). This space extends halfway across the membrane with
84 a similar depth of around 23 Å in both (Fig. 2c and Extended Data Fig. 4b). On the level of the outer
85 leaflet, TMs 1, 2, and 5 of the N-domain and TMs 7, 8, and 11 of the C-domain pack tightly against each
86 other and thus shield the central cavity from the external space (Extended Data Fig. 4a). Notably, TMs
87 1, 4, and 7 exhibit disordered regions at their C-terminal ends, followed by short kinked helical motifs
88 designated TMs 1b, 4b, and 7b (Fig. 1c and Extended Data Fig. 3).

89 *Conformational difference between inward- and outward-facing structures of FLVCR2*

90 From the as-isolated FLVCR2 samples we were able to determine not only the inward-facing
91 conformations but also the outward-facing conformation from class averages of even particle
92 distribution (Fig. 2a and Extended Data Fig. 2a). The outward-facing conformation of FLVCR2 is
93 characterized by a cavity that is accessible from the external space created by a rocker-switch rigid-
94 body motion of the two domains (Fig. 2b,c and Supplementary Video 1). This motion shifts the outer
95 halves of all TMs away from the central axis, while the inner halves adopt an inward movement to
96 obstruct the exit (Fig. 2b). The cavities in outward- and inward-facing conformations are 7.4 Å and 8.6
97 Å wide at their respective openings (Fig. 2c). The wedge-like volume of both cavities is surrounded by
98 an uncharged and hydrophobic protein environment, lined by mostly conserved residues (Extended
99 Data Fig. 5). Compared to the inward-facing cavity, the outward-facing cavity demonstrates a more
100 restricted pathway within its central region. In this narrowed segment of the cavity, the channel ends
101 at W102 and Y325, two residues that are highly conserved in both FLVCR transporters (Fig. 2c and
102 Extended Data Fig. 4b and 5).

103

104 In line with an alternating-access model, the inward-facing conformation of FLVCR2 features a tightly-
105 sealed external gate. This is mainly achieved by the juxtaposition of TM1b (N-domain) and TM7b (C-
106 domain; Fig. 2c,d). The inter-domain interaction between these two motifs is stabilized by a hydrogen
107 bonding network consisting of two pseudo-symmetry-related asparagine residues (N110-N332), as well
108 as E343 (TM8) and N239 (EL5-6; Supplementary Fig. 2). Furthermore, we identified a stable inter-
109 domain salt bridge between D124 (TM2) and R333 (TM7b), presumably reinforcing the external
110 occlusion (Fig. 2c,d, and Supplementary Fig. 2). FLVCR1 appears to employ a similar gating mechanism
111 on its external side, given that all the residues involved in the hydrogen bonding network of FLVCR2 are
112 found to be highly conserved between these two paralogs (Extended Data Fig. 4b,c). However, the
113 D124-R333 salt bridge in FLVCR2 is not conserved in FLVCR1. While the location of the D147 residue in
114 FLVCR1 aligns with that of D124 in FLVCR2, FLVCR1 possesses a glutamine taking the position of the
115 arginine (Extended Data Fig. 4c).

116

117 During the transition from inward- to outward-facing conformation of FLVCR2, interactions contributing
118 to the external gate become disrupted, while the formation of the internal gate occludes the central
119 cavity from the internal side. TM4b of the N-domain moves in proximity to the N-terminal end of TM11
120 of the C-domain to establish a first level of occlusion (Fig. 2b,c). An interaction network consisting of
121 several hydrogen bonds and a salt bridge is found within this region (Fig. 2e). E435 (TM11) plays a
122 central and versatile role by stably forming a hydrogen bond with S203 (TM4b) and a concurrent salt
123 bridge with R200 (TM4b; Fig. 2e and Supplementary Fig. 2). An additional inter-domain hydrogen
124 bonding site is identified between S199 (TM4b) and S439 (TM11; Fig. 2e and Supplementary Fig. 2). In
125 the peripheral region, K372 and R374 (EL8-9) approach N209 (EL4-5) and S212 (TM5) to form hydrogen
126 bond pairs and thus block the lateral accessibility of the cavity (Fig. 2e and Supplementary Fig. 2). A
127 second level of occlusion was observed beneath the internal ends of TMs 4, 10 and 11, where H1 and
128 H3 are positioned in close proximity (Fig. 2c,f). Here, the backbone carbonyl group and amide nitrogen
129 of A283 (H1) form stable hydrogen bonds with N497 (H3) and Y431 (IL10-11), respectively (Fig. 2f and
130 Supplementary Fig. 2). Together with the loop connecting TMs 10 and 11, the two helical motifs H1
131 and H3 serve as a latch to secure the closure of the two domains on the internal side.

132 *Substrate-specificity and auxiliary binding sites*

133 The transport substrates of both FLVCR1 and FLVCR2 have been contested for decades[14–17]. Both
134 FLVCR1 and FLVCR2 were previously proposed to hold a function in heme transport. With the goal of
135 assessing their heme-binding capabilities and localizing the putative heme-binding site, we performed
136 cryo-EM experiments using heme as a potential substrate.

137

138 A central observation upon determining the structure of heme-supplemented FLVCR2 was that the
139 presence of heme resolved the conformational heterogeneity, fully driving the transporter into the
140 outward-facing conformation (Fig. 3a and Extended Data Fig. 2b). Surprisingly, no density features of
141 heme were noticeable within the central cavity. Instead, we observed a density corresponding to heme
142 in the vicinity of the N-terminus of TM1 on the internal side, where it replaces the density we assigned
143 as a lipid molecule in the apo outward-facing structure (Fig. 3a,b). The protein surface in this particular
144 region displays a patch of positive charges, suggesting the heme molecule to be held in place by the
145 formation of electrostatic interactions between its two propionate groups and the side chains of R81,
146 R82, and K273 (Fig. 3b and Extended Data Fig. 5d). The map density of bound heme in our structure
147 indicates local mobility in the heme position due to the absence of macrocycle rigidifying axial
148 coordination (Fig. 3b). By contrast, cryo-EM studies on FLVCR1 in the presence of heme did not reveal
149 any heme binding or notable conformational changes. It is to note that neither the cavity dimensions
150 nor the residues lining the central cavities of FLVCR1 and FLVCR2 suggest the existence of a heme-
151 binding pocket.

152

153 To further characterize the molecular nature of heme binding in FLVCR2, we carried out atomistic MD
154 simulations, focusing on FLVCR2 in a lipid bilayer composed of 75% palmitoyloleoyl
155 phosphatidylethanolamine (POPE) and 25% palmitoyloleoyl phosphatidylglycerol (POPG). To probe
156 possible binding into the transport pathway, we first placed a heme close to the cavity opening in the
157 outward-facing conformation. In the subsequent MD simulations, the heme immediately crossed the
158 solvent layer and periodic boundary to interact with the loop region on the internal side for the

159 remainder of the simulation (Supplementary Video 2). We then positioned heme on the inner side of
160 the bilayer near the binding site observed by cryo-EM at the N-terminus of TM1 (Fig. 2c). In all replicas,
161 the contact between heme and the R82 residue was lost early in the simulations as the heme
162 reoriented and was absorbed into the lipid bilayer. However, the contact between one of the
163 propionate groups and R83 was consistently maintained. Upon membrane insertion, the heme formed
164 additional contacts with other residues (Supplementary Fig. 3). Stable interactions were observed
165 between the methyl group of heme and I270 (TM6), as well as one of the propionate groups and K273
166 (TM6). Our MD simulation data, together with our structural findings, point to the existence of a heme-
167 binding site at the N-domain of FLVCR2, located near the inner surface of the membrane. This finding
168 is in line with previously reported results demonstrating heme-binding at the N-terminal segment of
169 FLVCR2[18].
170
171 Subsequently, we focused our attention on choline as a potential substrate of FLVCR1 and FLVCR2 based
172 on the characteristic tryptophan-tyrosine clusters observed at the presumed substrate-binding cavities
173 of FLVCR1 and FLVCR2, respectively. This chemical environment is found analogously in the prokaryotic
174 choline transporter LicB, as well as predicted models of eukaryotic choline transporters[19–21] (Extended
175 Data Fig. 6). Indeed, we obtained cryo-EM maps of choline-bound structures of FLVCR1 and FLVCR2 at
176 a resolution of 2.6 Å and 2.8 Å, respectively (Fig. 3d,e and Extended Data Fig. 2b and 3c). Both structures
177 were captured in the inward-facing conformation, suggesting that choline is also capable of resolving
178 the conformational heterogeneity in FLVCR2 by trapping it in an inward-facing substrate-bound state.
179 Intriguingly, this effect is opposite to that of heme described above. The choline-bound structures
180 exhibit a Cα r.m.s.d. of 0.688 Å (FLVCR1) and 1.002 Å (FLVCR2) to their respective apo inward-facing
181 structures. The choline-bound inward-facing structures of FLVCR1 and FLVCR2 resemble each other and
182 their substrate binding sites are found in analogous locations within the transporter scaffold. The
183 bound choline molecule is caged inside the central binding site between the two domains of the FLVCRs,
184 surrounded mainly by TMs 1, 2, 4, 5, 7, and 11 (Fig. 3d,e). The binding sites in the two transporters are
185 formed by a suite of conserved residues. The central coordinating tryptophan residue ($W102^{FLVCR1}$ and

186 W125^{FLVCR2}) of TM1 is located above the choline, constraining the diffusion of the molecule towards the
187 external gate. Two additional aromatic residues of TM7, one tyrosine (Y325 ^{FLVCR1} and Y349^{FLVCR2}) and
188 one phenylalanine (F348^{FLVCR1} and F324^{FLVCR2}), line the peripheral space of the binding site and restrict
189 the movement of the choline within the pocket. Our MD simulations demonstrate that the quaternary
190 ammonium group of choline stably interacts with the conserved tryptophan residue (W125^{FLVCR1} and
191 W102^{FLVCR2}), forming concomitant cation-π interactions with both the tryptophan and tyrosine residues
192 (Fig. 3f,g). The hydroxyl group of the choline molecule showed more versatile interactions. Two
193 asparagine residues identified near the hydroxyl group formed transient hydrogen bonds with choline
194 during our simulations. In addition, at least two interacting water molecules were consistently present
195 near the OH-group of the bound choline, which was predominantly oriented away from the conserved
196 tryptophan towards the solvent phase (Supplementary Fig. 4 and Supplementary Video 3). It is
197 noteworthy that all these coordinating residues are fully conserved in mammals, suggesting a
198 specialized role of FLVCRs in recognizing and transporting choline across species (Fig. 3h).
199
200 To gain further insights into the spectrum of substrate selectivity of FLVCR1 and FLVCR2, we performed
201 nano differential scanning fluorimetry (nanoDSF) using choline, phosphocholine, and betaine as
202 candidate substrates (Fig. 3i and Extended Data Fig. 7). For both transporters, strong quenching of
203 tryptophan fluorescence could be observed by the addition of choline, but not its structurally related
204 metabolites (Fig. 3i). We determined choline dissociation rate constants for FLVCR1 at 25.10 ± 1.26 μM
205 and FLVCR2 at 125.22 ± 4.87 μM[22]. Subsequently, we attempted to assess the kinetic properties of both
206 FLVCRs via a solid-supported membrane-based electrophysiological (SSME) approach (Fig. 3j). For both
207 transporters we observed a rapid increase in current upon application of choline, followed by a fast
208 current decay, which can be attributed to an electrogenic substrate binding induced pre-steady state
209 (PSS) event. However, only for FLVCR2, a second current phase was observed, revealing a much slower
210 decay time constant. This current phase is typical for transport events that slowly charge the membrane
211 capacitor in SSME experiments[23,24]. Despite the structural similarities described above, FLVCRs seem to
212 have different kinetic fingerprints that might either originate from subtle structural differences

213 identified at the termini of the two transporters, or specific requirements to their surrounding
214 environment. Further, our data indicate that FLVCR-facilitated choline transport displays no immediate
215 pH dependency within the physiological range tested in our assay (Extended Data Fig. 8). Thus, we
216 conclude that FLVCRs most likely represent choline-driven uniporters. We then determined choline
217 binding affinities based on the PSS peaks and obtained values of 0.52 ± 0.07 mM for FLVCR1 and 3.28
218 ± 0.31 mM for FLVCR2. While the absolute affinities deduced from the SSME experiments are weaker
219 than those from the more direct DSF measurements, which may reflect an underlying transport phase,
220 the relative values consistently demonstrate a similar 5- to 6-fold difference in choline affinity between
221 the two transporters[25]. We note that our DSF-derived binding affinities more likely reflect values that
222 are realistic in a biological setting, as plasma choline concentrations are relatively stable at 5-10 μM[26].

223 *Translocation pathway of choline in FLVCRs*

224 MFS transporters typically cycle between inward- and outward-facing conformations, facilitating
225 substrate translocation in an alternating-access manner. Substrate binding often plays a pivotal role in
226 eliciting the conformational transitions[27]. Our cryo-EM data support this mechanism for at least FLVCR2,
227 where we see a full transition from the outward-facing to inward-facing state upon choline binding.
228 Our MD simulations map the route for substrate entry along the pathway in the outward-facing
229 conformation of FLVCR2. After spontaneously diffusing into the opening, choline initially interacts with
230 several residues near the protein surface, mainly D124 (Supplementary Fig. 5). It sequentially
231 approaches the deeper recesses of the cavity, primarily engaging with conserved aromatic residues
232 W102 and Y325. In a particular entry event, we observed choline moving to a position below the W102
233 residue within the binding site, consistent with our observations in the choline-bound structure of
234 FLVCR2 (Supplementary Video 4).

235

236 The substantial global conformational changes triggered by choline further alter the local arrangement
237 of substrate-coordinating residues within the translocation pathway. The rearrangement of the binding
238 site results in a more constricted pocket, promoted by the inward movement of the conserved residues
239 closer to the choline molecule (Extended Data Fig. 9a). The repositioning of these residues, especially
240 of the aromatic side chains, restricts the accessibility of the binding pocket and promotes choline
241 capture and engulfment.

242

243 The choline-bound inward-facing conformations likely represent the pre-release phase during the
244 translocation. In their choline-bound structures, the cavities of both FLVCRs share common
245 characteristics, exhibiting a neutral interior but a negatively charged surface at the exit (Extended Data
246 Fig. 5b,e). FLVCR1 features a slightly smaller cavity volume of 513 $Å^3$ compared to 579 $Å^3$ of FLVCR2
247 (Extended Data Fig. 9b). In an inter-domain interaction site at the cavity opening, a serine residue of
248 TM4 ($S222^{FLVCR1}$ and $S199^{FLVCR2}$) and a glutamate side chain of TM11 ($E459^{FLVCR1}$ and $E435^{FLVCR2}$) remain
249 in close proximity even with the internal gate open (Extended Data Fig. 9c,d). While these conserved

250 residues may interact to limit pathway accessibility, a peripheral solvent-accessible channel emerging
251 from the internal space to the binding site reveals a semi-open translocation pathway in the choline-
252 bound inward-facing conformations of both transporters (Extended Data Fig. 9b).
253
254 In our MD simulations, we captured a spontaneous choline release event from FLVCR2 through the
255 semi-open pathway that would complete the translocation process (Supplementary Video 5). The
256 choline spontaneously left the binding site after ~700 ns, transited in steps through the half channel,
257 and then escaped into the solvent at ~900 ns. Our apo inward-facing structures plausibly illustrate the
258 following post-release states. We speculate that an event occurs during the substrate release process
259 in both FLVCRs, resulting in the dissipation of the conserved serine-glutamate interactions and causing
260 the full opening of the internal cavity. This is suggested by our observations that the distance between
261 the S-E residues expands in the apo inward-facing structures relative to the choline-bound states
262 (Δd_{FLVCR1} = 3.3 Å and Δd_{FLVCR2} = 5.2 Å; Fig. 2e, Extended Data Fig. 4d and 9c,d). A subtle conformational
263 transition takes place upon the release of the choline in both FLVCRs, manifested by a rigid-body shift
264 between two domains that moves the inner halves slightly away from the central axis perpendicular to
265 the membrane plane (Extended Data Fig. 9e,f). The rearrangement of the TMs results an increased
266 angle between the N-domain and C-domain, widening by 0.9° in FLVCR1 compared to 4.3° in FLVCR2.
267 Consequently, the central cavities become less compact, enlarging from volumes of 513 $Å^3$ and 579 $Å^3$
268 for FLVCR1 and FLVCR2, to 771 $Å^3$ and 1046 $Å^3$, respectively. Meanwhile, the molecular architecture of
269 the external gate remains largely unchanged in the post-release inward-facing states of both FLVCRs
270 (Fig. 2d, Extended Data Fig. 4c and 9c).
271
272 Choline binding and release events drive additional local rearrangements in the translocation pathway
273 of FLVCR2. The inward-facing apo structure of FLVCR2 reveals a distinct lateral opening of the pathway,
274 directed towards the inner membrane leaflet of the lipid bilayer (Extended Data Fig. 10). This channel,
275 located between TM5 (N-domain) and TM8 (C-domain), accommodates a lipid/detergent-like density
276 in the apo state, as observed in our cryo-EM results (Extended Data Fig. 10b). Yet, when choline is

277 present in the central cavity, residue F220 seals the opening and prevents the lipid/detergent-like
278 density from accessing the channel (Extended Data Fig. 10c). The relevance of this site for
279 environmental interactions was further supported during our simulations with FLVCR2, where lipid-
280 entering events were observed (Extended Data Fig. 10a). The displacement of F220 allowed one of the
281 lipid's acyl tails to enter and reside within this channel. Whether or not this might be connected to a
282 putative allosteric regulatory mechanism linked to lipid binding in FLVCR2 as observed in other MFS-
283 type transporters remains to be further investigated[28,29].

284 **Discussion**

285 FLVCR transporters were considered to be human heme transporters. In this study, we have determined
286 cryo-EM structures of FLVCR1 and FLVCR2 in distinct apo, heme and choline-bound states, providing
287 valuable insights into architecture, substrate interaction and conformational dynamics of these two
288 MFS transporters. Our data support previous studies regarding the heme-binding properties of FLVCR2,
289 yet clearly demonstrate that choline is the transport substrate of both FLVCRs. Based on our structural
290 findings, we suggest a rocker-switch alternating-access mechanism for the transport cycle of choline
291 import (Fig. 4). As the resting state, the apo outward-facing FLVCR2 conformation is set up for choline
292 binding from the external space. Substrate-induced conformational changes drive FLVCR2 towards its
293 inward-facing state. Finally, the choline will be released to the cytosol or the mitochondrial matrix,
294 depending on the sub-cellular localization of FLVCR1 and FLVCR2[18]. Subsequent to choline release,
295 FLVCRs will transition into their outward-facing state in order to re-initiate the transport cycle. Our
296 structural data did not reveal fully occluded conformations that are key features of alternating access.
297 Hence, we suspect that these occluded conformations exist only transiently and rapidly convert
298 towards either the inward- or outward-facing conformations.

299

300 Our findings suggest that FLVCRs act as uniporters, conducting facilitated diffusion across the
301 membrane. Uniporters conventionally utilize the chemical potential of substrates as the only energy
302 source driving the transport process thermodynamically[30]. This mechanism appears to match the
303 kinetic fingerprints of FLVCRs observed in the SSM-based assays. Our cryo-EM data also reveal that
304 choline-binding prompts the conformational transition in FLVCR2 from the outward-facing to the
305 inward-facing state without requiring additional energy inputs. Corroborating this finding, our MD
306 simulation of FLVCR2 captured several spontaneous entry events of choline into the cavity in the
307 outward-facing conformation, including a traverse below the central coordinating tryptophan residue,
308 reminiscent of the local binding environment in the inward-facing choline-bound state (Supplementary
309 Fig. 5 and Supplementary Video 4). Furthermore, we observed a release event of choline from the
310 inward-facing conformation of FLVCR2 (Supplementary Video 5).

While choline is the primary transport substrate for FLVCR2, it should be highlighted that heme can also induce conformational changes, albeit leading to the opposing outward-facing state. This concurs with the previous reports that FLVCR2 is capable of binding heme with the N-domain yet not transporting it[16,18,31]. As labile cytoplasmic heme is readily degraded by heme oxygenase, we anticipate that the heme interaction of FLVCR2 will be restricted to mitochondria where heme biogenesis takes place. We performed matrix targeting sequences (MTSs) predictions to identify the targeting sequence of FLVCR2[32]. The N-terminal region of FLVCR2 exhibits a propensity score comparable to that of proteins known to be trafficked to the mitochondria (Supplementary Fig. 6). Correspondingly, the endogenous FLVCR2 protein, originating from its chromosomal locus, has been previously reported to localize within mitochondria[18]. We conclude that the physiological role of FLVCR2 is most likely to act as a mitochondrial choline importer that may be regulated by the availability of heme within the mitochondrial matrix. In addition, our MD simulations revealed that a physiological mitochondrial membrane potential influences the rates of choline entry and release in FLVCR2, favoring inward-directed translocation of this positively charged substrate (Supplementary Fig. 7 and Supplementary Table 1). Choline import in rat kidney mitochondria was previously found to depend on the membrane potential, which matches with our observations[33]. In contrast to FLVCR2, FLVCR1 showed no binding or response to heme, and obtained a very low propensity score in the MTSs prediction (Supplementary Fig. 6). Combined with insights from genome-wide association study data, we presume that FLVCR1 acts as a plasma membrane-localized choline transporter[34].

The successful elucidations of FLVCR structures in their choline-bound state establish the SLC49 family as a new class of human choline transporters[20]. Despite the positive charge of choline, the fully conserved binding site in FLVCRs exhibits a neutral charge environment. As a result, the coordination of bound choline is predominantly mediated by the cation-π interaction formed between the trimethylammonium group of choline and conserved aromatic residues. In a similar manner, the bacterial choline transporter LicB features a binding site composed of six aromatic and one amide side

338 chains, including W17 of TM1 that corresponds to the critical coordinating tryptophan residues in
339 FLVCRs[19] (Extended Data Fig. 6a). We performed a comparative analysis using the AlphaFold2 structures
340 of other putative human choline transporters (Extended Data Fig. 6b-d). Our examination of these
341 structures reveals binding pockets containing aromatic residues. In the high-affinity choline transporter
342 SLC5A7, the putative binding pocket encompasses four tryptophan and two tyrosine residues,
343 potentially forming a cation-π trap. The CTL (SLC44) family members feature a unique fold and the exact
344 position of their binding site remains unclear due to the absence of high-resolution structures. However,
345 the putative pocket of human SLC44A1 suggests the involvement of a tyrosine residue in choline
346 coordination[35]. The SLC22 family members share the same MFS fold with FLVCRs, and their putative
347 binding site with a broad substrate spectrum also contains aromatic and amide side chains that are
348 potential participants in choline coordination[36]. Our structural findings and analyses suggest that
349 cation-π interactions may be a common principle for choline coordination. While the cation-π
350 interaction appears to be highly specific and selective for substrate coordination in FLVCRs, our data
351 suggest that the hydroxyl group of choline preferentially forms promiscuous and dynamic interactions
352 either with the surrounding protein environment, such as amide-containing residues, or with water
353 molecules.
354
355 Choline, an indispensable quaternary ammonium cation with water-soluble vitamin-like characteristics,
356 is vital for a myriad of biological processes[37]. Dietary choline uptake mediated by certain transporters
357 is necessary as our bodies have limited capacity for *de novo* synthesis[38]. Choline deficiency is linked to
358 a plethora of undesired health consequences, for instance, skeletal muscle atrophy and
359 neurodegenerative diseases[39]. Additionally, abnormal choline metabolism is emerging as a hallmark for
360 oncogenesis and pathological inflammatory conditions[20,40,41]. Disorders including PCARP and DBA
361 associated with FLVCR1 and the Fowler syndrome related to FLVCR2 might stem from choline deficiency
362 that leads to developmental or degenerative complications. In conjunction with the known
363 physiological importance of choline and our current findings, a link between defective FLVCR function
364 and the associated pathologies becomes evident. Choline stands as the precursor for essential

365 compounds, such as the membrane phospholipid phosphatidylcholine (PC), the neurotransmitter
366 acetylcholine, and the methyl group donor betaine[39]. Altered choline metabolism is apt to cause
367 abnormal cell proliferation and differentiation conditions, impacting especially the nervous and
368 hematologic systems due to disturbances in neurotransmitter synthesis and methylation activities[42,43].
369 Beyond these impacts, choline metabolism in macrophages also affects mitochondrial morphology and
370 metabolism[41]. The disruption of PC synthesis results in the destruction of mitochondrial cristae,
371 compelling cells to rely only on substrate-level phosphorylation for ATP production. A handful of animal
372 studies have further underscored the interplay between choline supplementation and brain
373 development, particularly in angiogenesis[44–47]. Choline deficiency has been linked to decreased DNA
374 methylation within the promoters of genes that are important regulators of angiogenesis[44]. Moreover,
375 dysfunctional mutations or complete loss of choline transporters SLC5A7 or SLC44A1 have been
376 implicated in certain neurodegenerative conditions, including but not limited to distal hereditary motor
377 neuronopathy, congenital myasthenic syndrome, and childhood-onset neurodegeneration[48–52]. The
378 precise molecular mechanisms linking choline transport to these disorders are not yet fully deciphered
379 and require further study given their clinical implications.

380 **Online Methods**

381

382 **Generation of Inducible HEK293 Stable Cell Lines.**

383 The complementary DNAs of full-length wildtype FLVCR1 (human SLC49A1, NCBI Reference Sequence
384 NM_014053) and FLVCR2 (human SLC49A2, NCBI Reference Sequence: NM_017791) were cloned into
385 pcDNA5/FRT/TO (Invitrogen) vectors, respectively. The gene for both FLVCRs was modified by a C-
386 terminal FLAG fusion tag. Further details are found in sequence data provided as supplementary
387 information (Supplementary Tables 2 and 3). The recombinant Flp-In T-REx293-FLVCR1 and Flp-In T-
388 REx293-FLVCR2 cell lines were generated by using a tetracycline-inducible and commercially available
389 Flp-In T-REx host-cell line system from Invitrogen. Flp-In T-REx293 cells were cultured in high-glucose
390 Dulbecco's Modified Eagle's Medium (DMEM; Sigma-Aldrich) supplemented with 10% fetal bovine
391 serum (FBS; Gibco), 1% Pen/Strep (Gibco), 1 μg ml^{-1} Zeocin (Thermo Fisher), and 15 μg ml^{-1} blasticidin
392 S hydrochloride (AppliChem) at 37 °C in an atmosphere of 5% CO_2. Cells were not tested for
393 mycoplasma contamination. For stable integration, the pcDNA5/FRT-FLVCR1-FLAG and pcDNA5/FRT-
394 FLVCR2-FLAG vectors were cotransfected with the Flp recombinase encoding expression vector pOG44
395 (Thermo Fisher) at a 1:13 mass ratio, respectively. All transfection procedures were performed with
396 Lipofectamine™ 2000 reagent according to the manufacturer's instructions (Thermo Fisher). To select
397 stable clones, transfected cells were cultivated with growth medium containing 100 μg ml^{-1} hygromycin
398 B (AppliChem).

399

400 **Production and Purification of the human FLVCR1 and FLVCR2.**

401 For protein production, the Flp-In T-REx293-FLVCR1 and Flp-In T-REx293-FLVCR2 cell lines were cultured
402 in roller bottles (Greiner Bio-One) in growth media containing 100 μg ml^{-1} hygromycin B for 14 d under
403 the above-mentioned conditions. Gene expression was induced at 100% confluence by adding a final
404 concentration of 2 μg ml^{-1} doxycycline hydrochloride. After 72 h, cells were harvested with Accutase
405 solution (Sigma-Aldrich) and stored at −80 °C until further use. Harvested cells were suspended in cold
406 lysis buffer containing 25 mM Tris pH 7.4, 150 mM NaCl, and 0.1 g ml^{-1} SigmaFast

407 ethylenediaminetetraacetic acid (EDTA)-free protease inhibitor (Sigma-Aldrich) and disrupted by
408 stirring under high-pressure nitrogen atmosphere (750 MPa) for 45 min at 4 °C in a cell-disruption
409 vessel (Parr Instrument). The cell lysate was centrifuged at 8,000*g* at 4 °C for 15 min. Subsequently, the
410 low-velocity supernatant was centrifuged at 220,000*g* at 4 °C for 60 min. Pelleted membranes were
411 resuspended and stored in a storage buffer containing 25 mM Tris pH 7.4, 150 mM NaCl, 10% glycerol
412 (v/v), and 0.1 g ml^{-1} SigmaFast EDTA-free protease inhibitor (Sigma-Aldrich).
413
414 All purification steps of both FLVCRs were performed at 4 °C. Isolated membranes were solubilized with
415 1% (w/v) lauryl maltose neopentyl glycol (LMNG; GLYCON Biochemicals) with gentle stirring for 1 h.
416 The insoluble membrane fraction was removed via ultracentrifugation at 220,000*g* for 1 h.
417 Subsequently, the supernatant was incubated with ANTI-FLAG® M2 Affinity Gel resin (Merck) for 1 h.
418 The resin was preequilibrated with a buffer containing 50 mM Tris pH 7.4, 150 mM NaCl, and 0.02%
419 LMNG (w/v). The washing step was performed using 20 column volumes (CVs) of wash buffer [50 mM
420 Tris pH 7.4, 150 mM NaCl, 5% (v/v) glycerol, and 0.02% LMNG). The protein was eluted from the M2
421 resin with 10 CVs of the same buffer supplemented with 4 mM FLAG® Peptide (Merck). The eluted
422 sample was concentrated and subjected to a Superdex 200 Increase 10/300 column (GE Healthcare)
423 equilibrated with size exclusion chromatography (SEC) buffer [50 mM Tris pH 7.4, 150 mM NaCl, and
424 0.001% (w/v) LMNG]. Peak fractions were pooled, concentrated to 1.5 mg ml^{-1} using an Amicon 50-kDa
425 cut-off concentrator (Merck Millipore), and stored for further analysis.
426
427 For the dodecyl maltoside (DDM) and cholesterol hemisuccinate (CHS) solubilized samples used for
428 proteoliposome reconstitution, the proteins were purified based on the same protocol. The membrane
429 solubilization buffer contains 1% (w/v) DDM/0.2% (w/v) CHS instead of LMNG. Similarly, the wash
430 buffer contains 0.1% (w/v) DDM/0.02% (w/v) CHS, and the SEC buffer contains 0.02% (w/v) DDM/0.004%
431 (w/v) CHS.
432
433 **Immunoblotting**

434 Affinity-purified proteins were subjected to SDS-PAGE and immunoblotting. FLAG-tagged FLVCR1 and
435 FLVCR2 were detected using anti-FLAG (F3165, Sigma-Aldrich) antibodies at 1:1,000 dilution. Anti-
436 mouse IgG antibody conjugated with alkaline phosphatase (A9316, Sigma-Aldrich) was used as
437 secondary antibody at 1:5,000 dilution.
438
439 **Nano differential scanning fluorimetry (nanoDSF)**
440 NanoDSF measurements were carried out using Prometheus Panta (NanoTemper Technologies).
441 Purified protein samples were diluted with DSF buffer containing 50 mM HEPES pH 7.4, 150 mM NaCl,
442 and 0.001% (w/v) LMNG to 1 μM. Buffers with different concentrations of choline, phosphocholine, or
443 betaine were prepared by serial dilutions of DSF buffer containing 4 mM of the compounds. The protein
444 samples were mixed with an equal volume of DSF buffer or the compound-containing buffer with a
445 final protein concentration of 0.5 μM and then incubated at room temperature for 15 min. A volume
446 of 10 μl mixed solution was used per Prometheus high sensitivity capillary (NanoTemper Technologies).
447 A temperature ramp of 1 °C min^{-1} from 25 to 95 °C was applied while the intrinsic protein fluorescence
448 at 330 and 350 nm was recorded. Analysis of the initial ratio of F_{350}/F_{330} was carried out using Python
449 libraries including pandas, numpy, scipy and seaborn in Visual Studio Code (Microsoft). Three technical
450 replicates were recorded for data analysis.
451
452 **Proteoliposome preparation**
453 1-palmitoyl-2-oleoyl-sn-glycero-3-phosphoethanolamine (POPE, Avanti) and 1-Palmitoyl-2-oleoyl-*sn*-
454 glycero-3-phospho-(1'-rac-glycerol) (POPG, Avanti) in chloroform (25mg ml^{-1}) were mixed at the ratio
455 of 3:1 (w/w), followed by gentle evaporation of the chloroform and overnight desiccation under a
456 stream of nitrogen gas. The dried lipids were suspended in internal buffer comprised of 50 mM HEPES
457 pH 7.4, 150 mM NaCl to a final concentration of 12.5 mg ml^{-1} and sonicated until homogenous. The
458 lipid solution was subjected to three freeze-thaw cycles and extruded through a 400-nm polycarbonate
459 filter (Avestin) to generate unilamellar vesicles. The liposomes were destabilized by the addition of 0.13%
460 (w/v) Triton-X100 (Sigma) at room temperature. Purified DDM/CHS-solubilized FLVCR1 or FLVCR2

461 samples was added at a 1:50 protein-to-lipid mass ratio and incubated for 15 min at 4 °C. Protein-free
462 liposomes were prepared in parallel using the same concentration of DDM/CHS. The detergent was
463 removed by several additions of SM2-BioBeads (Bio-Rad). Firstly, 0.05 g ml^{-1} of BioBeads were added
464 to the sample and incubated with gentle agitation for 1 h at 4 °C, then 0.05 g ml^{-1} BioBeads were added
465 followed by incubation overnight at 4 °C, and finally 0.08 g ml^{-1} BioBeads were added with 2-h
466 incubation at 4 °C. BioBeads were removed by filtration and liposomes were collected by
467 ultracentrifugation at 264,000*g* for 20 min and resuspended at a concentration of 8 mg ml^{-1} lipids in
468 internal buffer. The reconstituted liposomes were flash frozen in liquid nitrogen and stored at −80 °C.
469

470 **SSM-based electrophysiology (SSME) assays**

471 SSM-based electrophysiology was performed on a SURFE^{2}R N1[53] (Nanion Technologies). For all
472 experiments, preparation of 3-mm sensors was performed as described[54]. For measurements, a single
473 solution exchange configuration was employed that consisted of three phases of 0.5 s duration each:
474 flow of non-activating solution (NA), activating solution (A), and non-activating solution (NA). Both NA
475 and A were prepared from the same main buffer (30 mM HEPES, 30 mM MES, and 300 mM NaCl at pH
476 7.4), while A was supplemented with choline chloride and NA was prepared by adding NaCl in an
477 equimolar manner. For the choline dose response curve, 50 mM choline chloride and 50 mM NaCl were
478 used to achieve A0 and NA (with the highest salt concentration), followed by dilution of A0 using NA
479 to generate all A solutions with choline concentrations ranging between 50 to 0.02 mM choline, while
480 keeping the total osmolarity constant. Proteoliposomes or liposomes (negative control) were thawed
481 and diluted 1:5 in NA, and sonicated using a bath sonicator for 20 s. A volume of 10 µl of the diluted
482 proteoliposomes were added to the sensors, and then centrifuged at 2,000*g* for 30 min. Assays were
483 performed on both sample and negative control to distinguish currents originating from FLVCRs and
484 artifact currents induced by the $choline^+/Na^+$ exchange due to interactions of the ions with the
485 membrane surface. Currents corresponding to different substrate concentrations were measured on
486 the same sensor, with a total of four different sensors. To determine transport kinetics of choline for
487 each FLVCR transporter, the measured currents for a given substrate concentration had the average

488 value of the corresponding negative control current subtracted from it. For the measurement at
489 different pH conditions, again the single solution exchange configuration was used. The main buffer
490 was titrated to different pH values that are physiologically relevant, ranging between 6 and 8, before
491 splitting into A supplemented with 15 mM choline chloride and the corresponding NA supplemented
492 with 15 mM NaCl. Before each measurement at a given pH, the pH was equilibrated via incubation for
493 3 minutes in NA solution at the given pH. Subsequently, peak currents were measured upon the
494 addition of A at the same pH. All pH values were measured sequentially using the same sensor, with a
495 total of four sensors. For both dose response curves and pH measurements, the error bars represent
496 the s.d. As the peak current signal can be a combined effect of electrogenic PSS and transport events[24],
497 we use the EC_{50} parameter to describe the concentration that generates the half maximum response.
498 Analysis of the data was performed in OriginPro (OriginLab Corporation).
499
500 **Cryo-EM sample preparation**
501 In order to collect cryo-EM data of FLVCR1 and FLVCR2 in different sample conditions, different
502 combinations of FLVCR proteins and putative substrate molecules were prepared. For both as-isolated
503 samples of FLVCRs, the protein concentration was adjusted to approximately 1.5 mg ml^{-1} and subjected
504 to plunge freezing. For samples supplemented with heme, heme loading was performed prior to the
505 SEC during protein purification with a 10-fold molar excess to the protein concentration. Peak fractions
506 were pooled and concentrated to 1.5 mg ml^{-1} before sample vitrification. For samples supplemented
507 with choline, purified proteins were adjusted to 1.5 mg ml^{-1} and choline was added at a final
508 concentration of 1 mM. The samples were incubated for 10 minutes at room temperature before
509 plunge freezing. Identical plunge freezing conditions were applied for all samples: Quantifoil R1.2/1.3
510 copper grids (mesh 300) were washed in chloroform and subsequently glow-discharged with a PELCO
511 easiGlow device at 15 mA for 90 seconds. A volume of 4 µl sample was applied to a grid and blotting
512 was performed for 4 seconds at 4 °C, 100% humidity with nominal blot force 20 immediately before
513 freezing in liquid ethane, using a Vitrobot Mark IV device (Thermo Scientific).
514

515 **Cryo-EM image recording**

516 For each cryo-EM sample, a dataset was recorded in Energy-Filtered Transmission Electron Microscopy
517 (EF-TEM) mode using either a Titan Krios G3i or a Krios G4 microscope (Thermo Scientific), both
518 operated at 300 kV. Electron-optical alignments were adjusted with EPU 3.0 - 3.4 (Thermo Scientific).
519 Images were recorded using automation strategies of EPU 3.0 - 3.4 in electron counting mode with
520 either a Gatan K3 (installed on Krios G3i) or a Falcon4 (installed on Krios G4) direct electron detector.
521 For Gatan K3 detector, a nominal magnification of 105,000, corresponding to a calibrated pixel size of
522 0.837 Å was applied, and dose fractionated movies (80 frames) were recorded at an electron flux of
523 approximately 15 e^- x $pixel^{-1}$ x s^{-1} for 4 s, corresponding to a total dose of ~80 e^-/A^2. For Falcon4 detector,
524 a nominal magnification of 215,000, corresponding to a calibrated pixel size 0.573 Å was applied, dose
525 fractionated movies were recorded in electron-event representation (EER) format at an electron flux
526 of approximately 4 e^- x $pixel^{-1}$ x s^{-1} for 5 s, corresponding to a total dose of ~50 e^-/A^2. Images were
527 recorded between -1.1 and -2.0 µm nominal defocus. Data collection quality was monitored through
528 EPU v. 3.0-3.4 and CryoSparc Live (versions 3.0 and 4.0)[55].

529

530 **Cryo-EM image processing**

531 For each acquired dataset, the same cryo-EM image processing approach was applied: MotionCor2 was
532 used to correct for beam-induced motion and to generate dose-weighted images[56]. Gctf was used to
533 determine the contrast transfer function (CTF) parameters and perform correction steps[57]. Images with
534 estimated poor resolution (>4 Å) and severe astigmatism (>400 Å) were removed at this step. Particles
535 were picked by TOPAZ and used for all further processing steps[58]. 2D classification, initial model
536 generation, 3D classification, CTF refinement, Bayesian polishing, 3D sorting, and final map
537 reconstructions were performed using RELION (versions 3.1 and 4.0) or cryoSPARC (versions 3.0 and
538 4.0)[55,59,60]. Fourier shell correlation (FSC) curves and local-resolution estimation were generated in
539 RELION or cryoSPARC for individual final maps. A schematic overview of our processing workflow, and
540 a summary of map qualities are shown in Extended Data Figs. 1-3, and Supplementary Table 4.

541

542 **Model building and geometry refinement**

543 The first atomic model of FLVCR1 and FLVCR2 were built into the respective EM density maps of the as-
544 isolated state in Coot (version 0.8) or ISOLDE within ChimeraX (version 1.5 and 1.6)[61–63], using the
545 AlphaFold predicted structures as initial templates[21]. After manual backbone tracing and docking of
546 side chains, real-space refinement in Phenix was performed (version 1.18)[64]. Refinement results were
547 manually inspected and corrected if required. This model was used as a template to build all
548 subsequent atomic models. The finalized models were validated by MolProbity implemented in
549 Phenix[65]. Map-to-model cross-validation was performed in Phenix (version 1.18). $FSC_{0.5}$ was used as
550 cut-off to define resolution. A summary of model parameters and the corresponding cryo-EM map
551 statistics is found in Supplementary Table 4. The finalized models were visualized using ChimeraX. The
552 built models of both FLVCR proteins in different states were used as starting structures for MD
553 simulations.

554

555 **Molecular dynamics simulations**

556 All simulations were run using GROMACS 2022.4[66]. The protein structures were embedded in a lipid
557 bilayer with 75% POPE and 25% POPG with CHARMM-GUI[67] and solvated in TIP3P water with 150 mM
558 NaCl. The charmm36m force field[68] was used with the improved WYF parameter set for cation-pi
559 interactions[69]. Initial systems were minimized for 5000 steepest descend steps and equilibrated for 450
560 ps of MD in an NVT ensemble and for 1.5 ns in an NPT ensemble. Position restraints of 4000 and 2000
561 kJ mol^{-1} nm^{-2} in the backbone and side chain heavy atoms, respectively, were gradually released during
562 equilibration. The z-positions of membrane phosphates, as well as lipid dihedrals, were initially
563 restrained with force constants of 1000 kJ mol^{-1} nm^{-2} and 1000 kJ mol^{-1} rad^{-2}, respectively, which were
564 gradually released during equilibration. The initial time step of 1 fs was increased to 2 fs during NPT
565 equilibration. Long range electrostatic interactions were treated with particle-mesh Ewald (PME) with
566 a cut-off of 1.2 nm[70]. Van-der-Waals interactions were cut off beyond a distance of 1.2 nm. The LINCS
567 algorithm was used to constrain the bonds involving hydrogen atoms[71]. During equilibration, a constant
568 temperature of 310 K was maintained with the Berendsen thermostat, using a coupling constant of 1

ps[72]. Constant pressure of 1 bar was established with a semi-isotropic Berendsen barostat and a coupling constant of 5 ps. In the production runs, a Nosé–Hoover thermostat and a Parrinello–Rahman barostat were used[73,74].

We used our cryo-EM structures as initial models for simulations of apo and choline-bound inward-facing FLVCR1, apo and choline-bound inward-facing FLVCR2, and apo outward-facing FLVCR2. An initial structure of choline-bound outward-facing FLVCR2 was generated aligning apo outward-facing FLVCR2 to choline-bound inward-facing FLVCR2 and maintaining choline in the cavity. In choline entry simulations, the apo structures were used with 380 mM choline in solution. Simulations of heme-bound outward- and inward-facing FLVCR2 were prepared by manually placing heme close to the observed binding region in the N-terminus of the apo structures, outside of the lipid bilayer. Additionally, a simulation of FLVCR2 in the outward-facing conformation was conducted, with the heme initially positioned in front of the cavity entrance. Three replicas with random initial velocities from the Boltzmann distribution were run for the rest of the systems. Choline release simulations were interrupted after choline exit from the cavity, and hence have variable duration. For all other systems, each replica was run for 1 μs. To reproduce mitochondrial membrane potential, an additional set of simulations was run for choline-bound inward- and outward-facing, and apo outward-facing FLVCR2 with choline in solution, in which an electric field of -200 mV was applied in the z-dimension.

Visual Molecular Dynamics (VMD) and MDAnalysis were used to visualize and analyze the trajectories, respectively[75,76].

Interior tunnels and cavities

Tunnels and cavities were mapped with MOLE 2.5 with a bottleneck radius of 1.2 Å, bottleneck tolerance 3 Å, origin radius 5 Å, surface radius 10 Å, probe radius 5 Å and an interior threshold of 1.1 Å[77].

595 We calculated the volume of the cavity using CASTp with a bottleneck radius of 1.4 Å. Residues 297-
596 320 and 512-516 were removed from the FLVCR1 model to avoid the misattribution of the volume
597 between internal loops to the cavity volume[78]. Analogously, residues 272-296 and 487-502 were not
598 included in the cavity volume calculation of FLVCR2.
599
600 **Multiple sequence alignments**
601 Multiple sequence alignments of FLVCR1 and FLVCR2 from *homo sapiens*, *Felis catus*, *Mus musculus*,
602 and *Sus scrofa* were performed using Clustal Omega[79].

603 **Data availability**

604 Cryo-EM maps are deposited at the Electron Microscopy Data Bank under accession numbers: EMD-
605 18334, EMD-18335, EMD-18336, EMD-18337, EMD-18338, EMD-18339. Atomic models of human
606 FLVCR1 and FLVCR2 have been deposited to the Protein Data Bank under accession numbers: 8QCS,
607 8QCT, 8QCX, 8QCY, 8QCZ, 8QD0. All other data is presented in the main text or supplementary materials.
608 Source data are provided with this paper.

609

610 **Acknowledgements**

611 We thank Hartmut Michel for support and providing infrastructural resources. We thank ChatGPT by
612 OpenAI for assistance with language editing and polishing of the manuscript. We thank the Central
613 Electron Microscopy Facility at MPI of Biophysics for technical support and access to instrumentation.

614

615 **Funding**

616 This work was supported by the Max Planck Society and the Nobel Laureate Fellowship of the Max
617 Planck Society.

618

619 **Author contributions**

620 T-H.W. purified proteins, performed biochemical assays, prepared grids, collected cryo-EM data,
621 processed cryo-EM data, refined the structure, built the model, co-drafted the manuscript, and
622 prepared figures. A.C.C. performed MD simulations, analyzed data, co-drafted the manuscript, and
623 prepared figures. W.J. performed cell productions, optimized purification conditions, and purified
624 proteins. A.B. performed SSM-based assays, analyzed data, and prepared figures. S.W. calibrated and
625 aligned the microscope. G.G. assisted in cell culturing and protein purification. G.H., D.W., and S.S.
626 supervised the project. D.W. implemented cell production and protein purification, prepared grids,
627 performed initial cryo-EM screening experiments, collected cryo-EM data, analyzed data, drafted the
628 manuscript, and funded the project. D.W. and S.S. initiated the project. S.S. designed research,
629 evaluated data, funded the project, drafted the manuscript, and generated figures.

630

631 **Competing interests**

632 The authors declare no conflict-of-interest.

633

634 **References**

635 1. Khan, A. A. & Quigley, J. G. Heme and FLVCR-related transporter families SLC48 and SLC49. *Mol.*
636 *Asp. Med.* **34**, 669–682 (2013).

637 2. Tailor, C. S., Willett, B. J. & Kabat, D. A putative cell surface receptor for anemia-inducing feline
638 leukemia virus subgroup C is a member of a transporter superfamily. *J. Virol.* **73**, 6500–5 (1999).

639 3. Brown, J. K., Fung, C. & Tailor, C. S. Comprehensive Mapping of Receptor-Functioning Domains in
640 Feline Leukemia Virus Subgroup C Receptor FLVCR1. *J. Virol.* **80**, 1742–1751 (2006).

641 4. Dutt, S., Hamza, I. & Bartnikas, T. B. Molecular Mechanisms of Iron and Heme Metabolism. *Annu.*
642 *Rev. Nutr.* **42**, 311–335 (2022).

643 5. Rajadhyaksha, A. M. *et al.* Mutations in FLVCR1 Cause Posterior Column Ataxia and Retinitis
644 Pigmentosa. *Am. J. Hum. Genet.* **87**, 643–654 (2010).

645 6. Rey, M. A. *et al.* Enhanced alternative splicing of the FLVCR1 gene in Diamond Blackfan anemia
646 disrupts FLVCR1 expression and function that are critical for erythropoiesis. *Haematologica* **93**, 1617–
647 1626 (2008).

648 7. Meyer, E. *et al.* Mutations in FLVCR2 Are Associated with Proliferative Vasculopathy and
649 Hydranencephaly-Hydrocephaly Syndrome (Fowler Syndrome). *Am. J. Hum. Genet.* **86**, 471–478
650 (2010).

651 8. Thomas, S. *et al.* High-throughput sequencing of a 4.1 Mb linkage interval reveals FLVCR2 deletions
652 and mutations in lethal cerebral vasculopathy. *Hum. Mutat.* **31**, 1134–1141 (2010).

653 9. Petrillo, S. *et al.* Endothelial cells require functional FLVCR1a during developmental and adult
654 angiogenesis. *Angiogenesis* 1–20 (2023) doi:10.1007/s10456-023-09865-w.

655 10. Santander, N. *et al.* Lack of Flvcr2 impairs brain angiogenesis without affecting the blood-brain
656 barrier. *J. Clin. Investig.* **130**, 4055–4068 (2020).

657 11. Peng, C. *et al.* FLVCR1 promotes the proliferation and tumorigenicity of synovial sarcoma through
658 inhibiting apoptosis and autophagy. *Int. J. Oncol.* **52**, 1559–1568 (2018).

659 12. Su, X. *et al.* The prognostic marker FLVCR2 associated with tumor progression and immune
660 infiltration for acute myeloid leukemia. *Front. Cell Dev. Biol.* **10**, 978786 (2022).

661 13. Yan, N. Structural Biology of the Major Facilitator Superfamily Transporters. *Annu. Rev. Biophys.*
662 **44**, 257–283 (2015).
663 14. Quigley, J. G. *et al.* Identification of a Human Heme Exporter that Is Essential for Erythropoiesis.
664 *Cell* **118**, 757–766 (2004).
665 15. Duffy, S. P. *et al.* The Fowler Syndrome-Associated Protein FLVCR2 Is an Importer of Heme. *Mol.*
666 *Cell. Biol.* **30**, 5318–5324 (2010).
667 16. Yuan, X., Protchenko, O., Philpott, C. C. & Hamza, I. Topologically Conserved Residues Direct Heme
668 Transport in HRG-1-related Proteins*. *J. Biol. Chem.* **287**, 4914–4924 (2012).
669 17. Ponka, P., Sheftel, A. D., English, A. M., Bohle, D. S. & Garcia-Santos, D. Do Mammalian Cells Really
670 Need to Export and Import Heme? *Trends Biochem. Sci.* **42**, 395–406 (2017).
671 18. Li, Y. *et al.* MFSD7C switches mitochondrial ATP synthesis to thermogenesis in response to heme.
672 *Nat. Commun.* **11**, 4837 (2020).
673 19. Bärland, N. *et al.* Mechanistic basis of choline import involved in teichoic acids and
674 lipopolysaccharide modification. *Sci. Adv.* **8**, eabm1122 (2022).
675 20. Glunde, K., Bhujwalla, Z. M. & Ronen, S. M. Choline metabolism in malignant transformation. *Nat.*
676 *Rev. Cancer* **11**, 835–848 (2011).
677 21. Jumper, J. *et al.* Highly accurate protein structure prediction with AlphaFold. *Nature* **596**, 583–589
678 (2021).
679 22. Perez, C. *et al.* Substrate-bound outward-open state of the betaine transporter BetP provides
680 insights into Na+ coupling. *Nat. Commun.* **5**, 4231 (2014).
681 23. Bazzone, A. *et al.* Investigation of sugar binding kinetics of the E. coli sugar/H+ symporter XylE
682 using solid-supported membrane-based electrophysiology. *J. Biol. Chem.* **298**, 101505 (2022).
683 24. Bazzone, A., Zerlotti, R., Barthmes, M. & Fertig, N. Functional characterization of SGLT1 using
684 SSM-based electrophysiology: Kinetics of sugar binding and translocation. *Front. Physiol.* **14**, 1058583
685 (2023).
686 25. Bazzone, A. *et al.* SSM-based electrophysiology, a label-free real-time method reveals sugar
687 binding & transport events in SGLT1. *Biosens. Bioelectron.* **197**, 113763 (2022).

688 26. Sarter, M. & Parikh, V. Choline transporters, cholinergic transmission and cognition. *Nat. Rev.*
689 *Neurosci.* **6**, 48–56 (2005).
690 27. Drew, D., North, R. A., Nagarathinam, K. & Tanabe, M. Structures and General Transport
691 Mechanisms by the Major Facilitator Superfamily (MFS). *Chem. Rev.* **121**, 5289–5335 (2021).
692 28. Martens, C. *et al.* Direct protein-lipid interactions shape the conformational landscape of
693 secondary transporters. *Nat. Commun.* **9**, 4151 (2018).
694 29. Corradi, V. *et al.* Emerging Diversity in Lipid–Protein Interactions. *Chem. Rev.* **119**, 5775–5848
695 (2019).
696 30. Zhang, X. C. & Han, L. Uniporter substrate binding and transport: reformulating mechanistic
697 questions. *Biophys. Rep.* **2**, 45–54 (2016).
698 31. Kalailingam, P. *et al.* Deficiency of MFSD7c results in microcephaly-associated vasculopathy in
699 Fowler syndrome. *J. Clin. Investig.* **130**, 4081–4093 (2020).
700 32. Schneider, K., Zimmer, D., Nielsen, H., Herrmann, J. M. & Mühlhaus, T. iMLP, a predictor for
701 internal matrix targeting-like sequences in mitochondrial proteins. *Biol. Chem.* **402**, 937–943 (2021).
702 33. O'Donoghue, N., Sweeney, T., Donagh, R., Clarke, K. J. & Porter, R. K. Control of choline oxidation
703 in rat kidney mitochondria. *Biochim. Biophys. Acta (BBA) - Bioenerg.* **1787**, 1135–1139 (2009).
704 34. Kenny, T. C. *et al.* Integrative genetic analysis identifies FLVCR1 as a plasma-membrane choline
705 transporter in mammals. *Cell Metab.* **35**, 1057-1071.e12 (2023).
706 35. Xie, T. *et al.* Rational exploration of fold atlas for human solute carrier proteins. *Structure* **30**,
707 1321-1330.e5 (2022).
708 36. Nigam, S. K. The SLC22 Transporter Family: A Paradigm for the Impact of Drug Transporters on
709 Metabolic Pathways, Signaling, and Disease. *Annu. Rev. Pharmacol. Toxicol.* **58**, 663–687 (2018).
710 37. Ueland, P. M. Choline and betaine in health and disease. *J. Inherit. Metab. Dis.* **34**, 3–15 (2011).
711 38. Zeisel, S. H. Choline: Critical Role During Fetal Development and Dietary Requirements in Adults.
712 *Annu. Rev. Nutr.* **26**, 229–250 (2006).
713 39. Goh, Y. Q., Cheam, G. & Wang, Y. Understanding Choline Bioavailability and Utilization: First Step
714 Toward Personalizing Choline Nutrition. *J. Agric. Food Chem.* **69**, 10774–10789 (2021).

715 40. Sanchez-Lopez, E. *et al.* Choline Uptake and Metabolism Modulate Macrophage IL-1β and IL-18
716 Production. *Cell Metab.* **29**, 1350-1362.e7 (2019).
717 41. Ghorbani, P. *et al.* Choline metabolism underpins macrophage IL-4 polarization and RELMα up-
718 regulation in helminth infection. (2022) doi:10.1101/2022.09.30.510305.
719 42. Bhat, S., El-Kasaby, A., Freissmuth, M. & Sucic, S. Functional and Biochemical Consequences of
720 Disease Variants in Neurotransmitter Transporters: A Special Emphasis on Folding and Trafficking
721 Deficits. *Pharmacol. Ther.* **222**, 107785–107785 (2021).
722 43. Wortmann, S. B. & Mayr, J. A. Choline-related-inherited metabolic diseases—A mini review. *J.*
723 *Inherit. Metab. Dis.* **42**, 237–242 (2019).
724 44. Mehedint, M. G., Craciunescu, C. N. & Zeisel, S. H. Maternal dietary choline deficiency alters
725 angiogenesis in fetal mouse hippocampus. *Proc. Natl. Acad. Sci.* **107**, 12834–12839 (2010).
726 45. King, J. H. *et al.* Maternal Choline Supplementation Modulates Placental Markers of Inflammation,
727 Angiogenesis, and Apoptosis in a Mouse Model of Placental Insufficiency. *Nutrients* **11**, 374 (2019).
728 46. Kwan, S. T. (Cecilia) *et al.* Maternal choline supplementation during murine pregnancy modulates
729 placental markers of inflammation, apoptosis and vascularization in a fetal sex-dependent manner.
730 *Placenta* **53**, 57–65 (2017).
731 47. Jin, X., Wang, R., Wang, H., Long, C. & Wang, H. Brain protection against ischemic stroke using
732 choline as a new molecular bypass treatment. *Acta Pharmacol. Sin.* **36**, 1416–1425 (2015).
733 48. Irobi, J., Jonghe, P. D. & Timmerman, V. Molecular genetics of distal hereditary motor
734 neuropathies. *Hum. Mol. Genet.* **13**, R195–R202 (2004).
735 49. Wang, H. *et al.* Choline transporter mutations in severe congenital myasthenic syndrome disrupt
736 transporter localization. *Brain* **140**, 2838–2850 (2017).
737 50. Fagerberg, C. R. *et al.* Choline transporter-like 1 deficiency causes a new type of childhood-onset
738 neurodegeneration. *Brain* **143**, 94–111 (2019).
739 51. Bauché, S. *et al.* Impaired Presynaptic High-Affinity Choline Transporter Causes a Congenital
740 Myasthenic Syndrome with Episodic Apnea. *Am. J. Hum. Genet.* **99**, 753–761 (2016).

741 52. Cruz, P. M. R. *et al.* Presynaptic congenital myasthenic syndrome due to three novel mutations in
742 SLC5A7 encoding the sodium-dependant high-affinity choline transporter. *Neuromuscul. Disord.* **31**,
743 21–28 (2021).
744 53. Bazzone, A., Barthmes, M. & Fendler, K. Chapter Two SSM-Based Electrophysiology for
745 Transporter Research. *Methods Enzym.* **594**, 31–83 (2017).
746 54. Bazzone, A. & Barthmes, M. Functional Characterization of SLC Transporters Using Solid
747 Supported Membranes. *Methods Mol. Biol. (Clifton, NJ)* **2168**, 73–103 (2020).
748 55. Punjani, A., Rubinstein, J. L., Fleet, D. J. & Brubaker, M. A. cryoSPARC: algorithms for rapid
749 unsupervised cryo-EM structure determination. *Nat. Methods* **14**, 290–296 (2017).
750 56. Zheng, S. Q. *et al.* MotionCor2: anisotropic correction of beam-induced motion for improved cryo-
751 electron microscopy. *Nat. Methods* **14**, 331–332 (2017).
752 57. Zhang, K. Gctf: Real-time CTF determination and correction. *J. Struct. Biol.* **193**, 1–12 (2016).
753 58. Bepler, T. *et al.* Positive-unlabeled convolutional neural networks for particle picking in cryo-
754 electron micrographs. *Nat. methods* **16**, 1153–1160 (2019).
755 59. Scheres, S. H. W. RELION: Implementation of a Bayesian approach to cryo-EM structure
756 determination. *J. Struct. Biol.* **180**, 519–530 (2012).
757 60. Kimanius, D., Dong, L., Sharov, G., Nakane, T. & Scheres, S. H. W. New tools for automated cryo-
758 EM single-particle analysis in RELION-4.0. *Biochem. J.* **478**, 4169–4185 (2021).
759 61. Emsley, P., Lohkamp, B., Scott, W. G. & Cowtan, K. Features and development of Coot. *Acta*
760 *Crystallogr. Sect. D* **66**, 486–501 (2010).
761 62. Croll, T. I. ISOLDE: a physically realistic environment for model building into low-resolution
762 electron-density maps. *Acta Crystallogr. Sect. D, Struct. Biol.* **74**, 519–530 (2018).
763 63. Goddard, T. D. *et al.* UCSF ChimeraX: Meeting modern challenges in visualization and analysis:
764 UCSF ChimeraX Visualization System. *Protein Sci.* **27**, 14–25 (2017).
765 64. Adams, P. D. *et al.* PHENIX: a comprehensive Python-based system for macromolecular structure
766 solution. *Acta Crystallogr. Sect. D, Biol. Crystallogr.* **66**, 213–21 (2009).

65. Chen, V. B. *et al.* MolProbity: all-atom structure validation for macromolecular crystallography. *Acta Crystallogr. Sect. D: Biol. Crystallogr.* **66**, 12–21 (2010).

66. Abraham, M. J. *et al.* GROMACS: High performance molecular simulations through multi-level parallelism from laptops to supercomputers. *SoftwareX* **1**, 19–25 (2015).

67. Jo, S., Kim, T., Iyer, V. G. & Im, W. CHARMM-GUI: A web-based graphical user interface for CHARMM. *J. Comput. Chem.* **29**, 1859–1865 (2008).

68. Huang, J. *et al.* CHARMM36m: an improved force field for folded and intrinsically disordered proteins. *Nat. Methods* **14**, 71–73 (2017).

69. Khan, H. M., MacKerell, A. D. & Reuter, N. Cation-π Interactions between Methylated Ammonium Groups and Tryptophan in the CHARMM36 Additive Force Field. *J. Chem. theory Comput.* **15**, 7–12 (2018).

70. Essmann, U. *et al.* A smooth particle mesh Ewald method. *J. Chem. Phys.* **103**, 8577–8593 (1995).

71. Hess, B., Bekker, H., Berendsen, H. J. C. & Fraaije, J. G. E. M. LINCS: A linear constraint solver for molecular simulations. *J. Comput. Chem.* **18**, 1463–1472 (1997).

72. Berendsen, H. J. C., Postma, J. P. M., Gunsteren, W. F. van, DiNola, A. & Haak, J. R. Molecular dynamics with coupling to an external bath. *J. Chem. Phys.* **81**, 3684–3690 (1984).

73. Evans, D. J. & Holian, B. L. The Nose–Hoover thermostat. *J. Chem. Phys.* **83**, 4069–4074 (1985).

74. Parrinello, M. & Rahman, A. Polymorphic transitions in single crystals: A new molecular dynamics method. *J. Appl. Phys.* **52**, 7182–7190 (1981).

75. Humphrey, W., Dalke, A. & Schulten, K. VMD: Visual molecular dynamics. *J. Mol. Graph.* **14**, 33–38 (1996).

76. Michaud-Agrawal, N., Denning, E. J., Woolf, T. B. & Beckstein, O. MDAnalysis: a toolkit for the analysis of molecular dynamics simulations. *J. Comput. Chem.* **32**, 2319–27 (2010).

77. Sehnal, D. *et al.* MOLE 2.0: advanced approach for analysis of biomacromolecular channels. *J. Cheminformatics* **5**, 39–39 (2013).

78. Tian, W., Chen, C., Lei, X., Zhao, J. & Liang, J. CASTp 3.0: computed atlas of surface topography of proteins. *Nucleic Acids Res.* **46**, W363–W367 (2018).

79. Sievers, F. *et al.* Fast, scalable generation of high-quality protein multiple sequence alignments using Clustal Omega. *Mol. Syst. Biol.* **7**, 539–539 (2011).

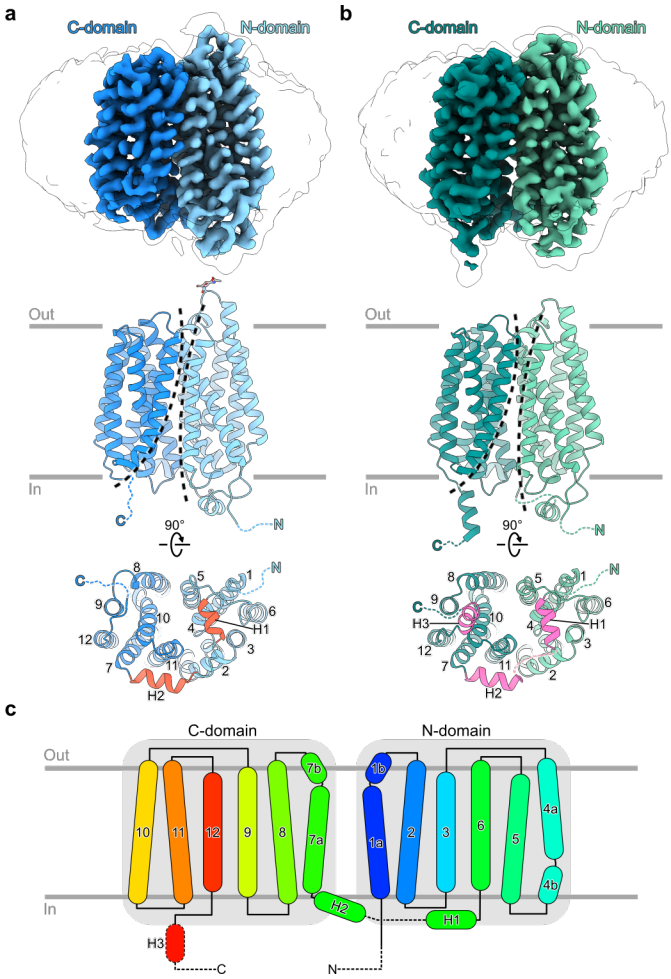

Fig. 1: Cryo-EM structures of FLVCR1 and FLVCR2 in their inward-facing state.

Cryo-EM density (top) and atomic model (middle and bottom) of inward-facing FLVCR1 (**a**), and inward-facing FLVCR2 (**b**). The N- and C-domains are coloured in different shades of blue and green for FLVCR1 and FLVCR2, respectively. A transparent cryo-EM density lowpass-filtered at 6 Å is shown to visualize the detergent belt surrounding the transmembrane region. The internal view (bottom) shows the arrangement of TMs, with inner side helices highlighted in orange (FLVCR1) or pink (FLVCR2). The sidechain of N265 in FLVCR1 and its N-linked glycan (grey) are shown as stick models. **c**, Schematic diagram of FLVCR family showing the topology of the secondary structure. Motifs that are not observed in both cryo-EM structures of FLVCR1 and FLVCR2 are shown as dashed lines.

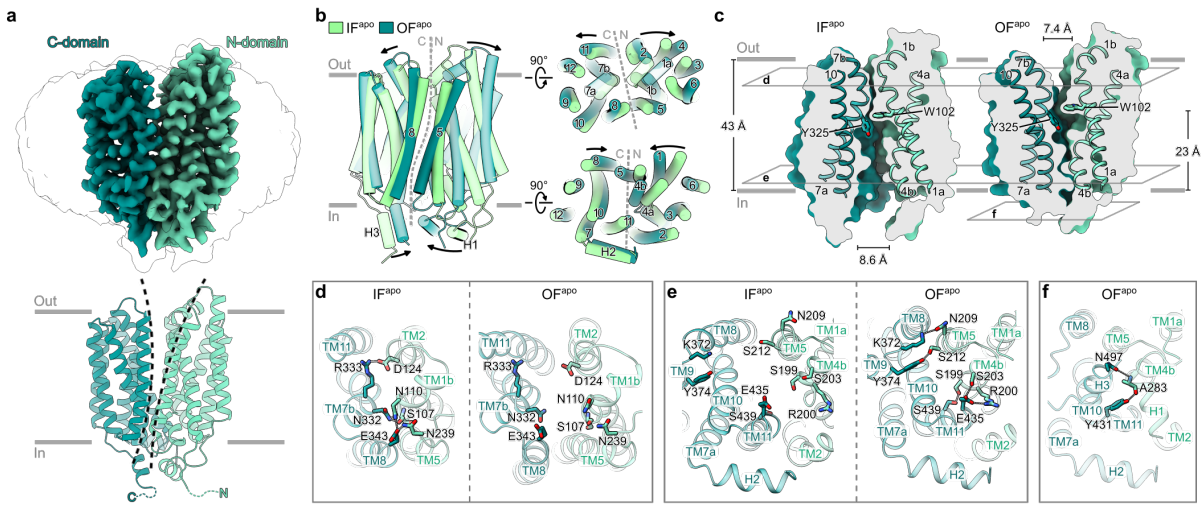

808

809 **Fig. 2: Structural heterogeneity and gating mechanism of FLVCR2.**

810 **a**, Cryo-EM density (top) and atomic model (bottom) of outward-facing FLVCR2. **b**, Structural
811 superposition of FLVCR2-OF^{apo} (dark green) and FLVCR2-IF^{apo} (light green). **c**, Cut-away views of the
812 surface representation showing the cavity shape of FLVCR2-IF^{apo} (left) and FLVCR2-OF^{apo} (right). Two
813 central aromatic residues are shown as sticks. Cross-sections of inter-domain interactions in FLVCR2-
814 IF^{apo} (left) and FLVCR2-OF^{apo} (right) are shown from the external (**d**), or from the internal side (**e**). **f**,
815 Internal view of FLVCR2-OF^{apo} showing the inter-domain interactions between H1 and H3. Residues
816 participating in the inter-domain interactions are shown as sticks; hydrogen bonds and salt bridges are
817 labelled with dashed lines.

818

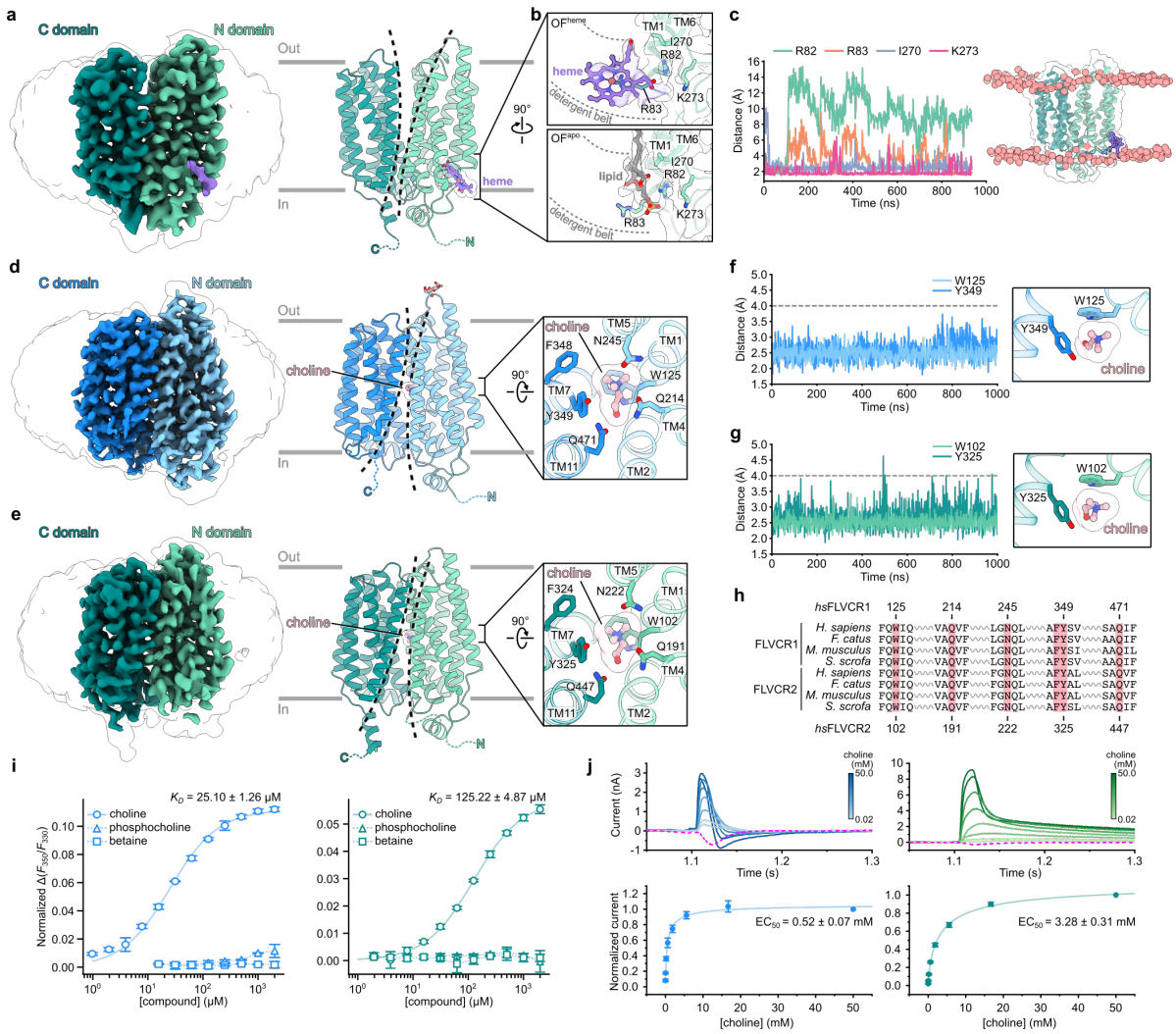

Fig. 3: Cryo-EM structures of FLVCR1 and FLVCR2 in complex with choline and heme.

a, Cryo-EM density (left) and ribbon model (right) of the heme-bound outward-facing FLVCR2 (FLVCR2-OF^{heme}). The heme molecule is shown in ball-and-stick representation, and the corresponding cryo-EM density is coloured in purple. **b**, Close-up views of the heme-binding site in FLVCR2-OF^{heme} (top) and in FLVCR2-OF^{apo} (bottom) with locally-filtered cryo-EM density. Residues in close proximity to heme are shown as sticks. A lipid molecule (grey ball-and-stick) is fitted into the lipid-like density at the heme-binding site of FLVCR2-OF^{apo}. **c**, Time-resolved distance plot between heme and interacting residues from MD experiments are shown. A snapshot of FLVCR2-heme interaction during the simulation is shown. For simplicity, only the phosphates of POPE/POPG are shown as red spheres. **d**,**e**, Cryo-EM densities and atomic models of the choline-bound inward-facing FLVCR1 (FLVCR1-IF^{choline}) structure, and the choline-bound inward-facing FLVCR2 (FLVCR2-IF^{choline}) structure, respectively. The bound choline is shown as ball-and-stick model; binding site residues are shown as sticks. **f**,**g**, Time-resolved

distance plots between choline and the highly-conserved tryptophan and tyrosine residues forming the choline-binding pockets of FLVCR1 (**f**) and FLVCR2 (**g**) obtained from MD simulation runs. A cation-π interaction is assumed for distance <4 Å (grey dashed line). **h**, Protein sequence alignment of choline-binding pocket residues (red block) in FLVCR1 and FLVCR2 across various mammalian species. Indicated residue numbers refer to FLVCR1 and FLVCR2 from *homo sapiens*. **i**, Choline-binding affinity of FLVCR1 (left) and FLVCR2 (right) determined by nanoDSF. Data are represented as mean ± standard deviation (s.d.; n = 3). **j**, Representative choline-induced current traces of FLVCR1 (left) or FLVCR2 (right) containing proteoliposomes. Representative current traces of protein-free liposomes induced by 50 mM choline are shown as magenta dashed lines. Data are represented as mean ± s.d. (n = 4).

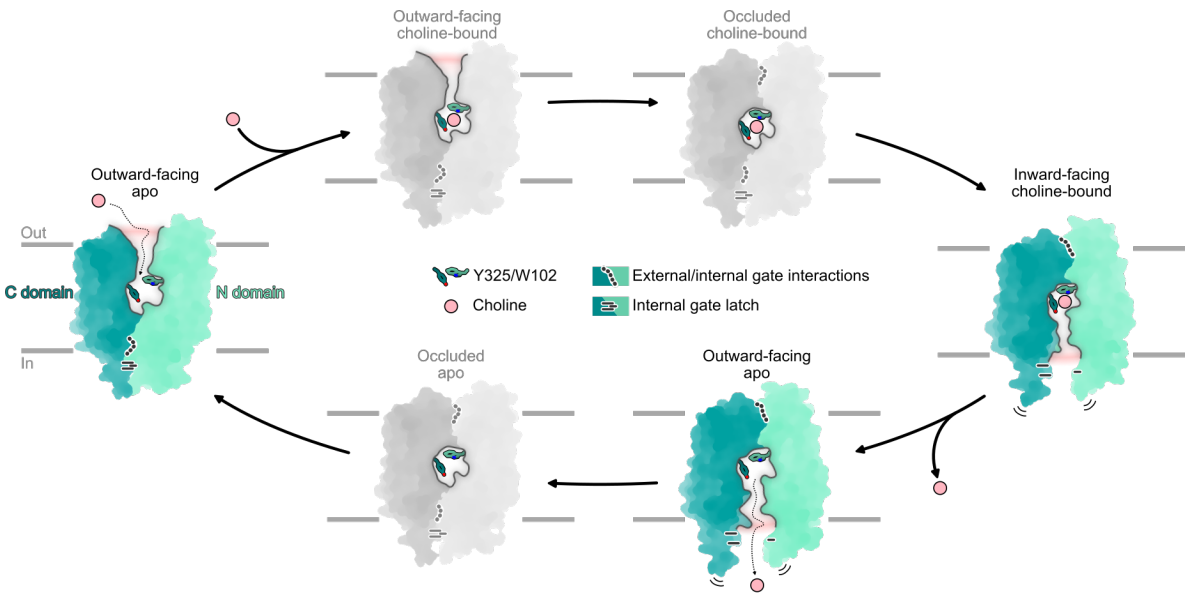

Fig. 4: Proposed model for choline transport by FLVCR2.

Schematic illustration of FLVCR2 conformations during the choline transport cycle. Green-coloured states represent experimentally obtained conformations in this study. States coloured in grey are hypothesized based on knowledge about the commonly characterized alternative-access mechanism of MFS transporters.

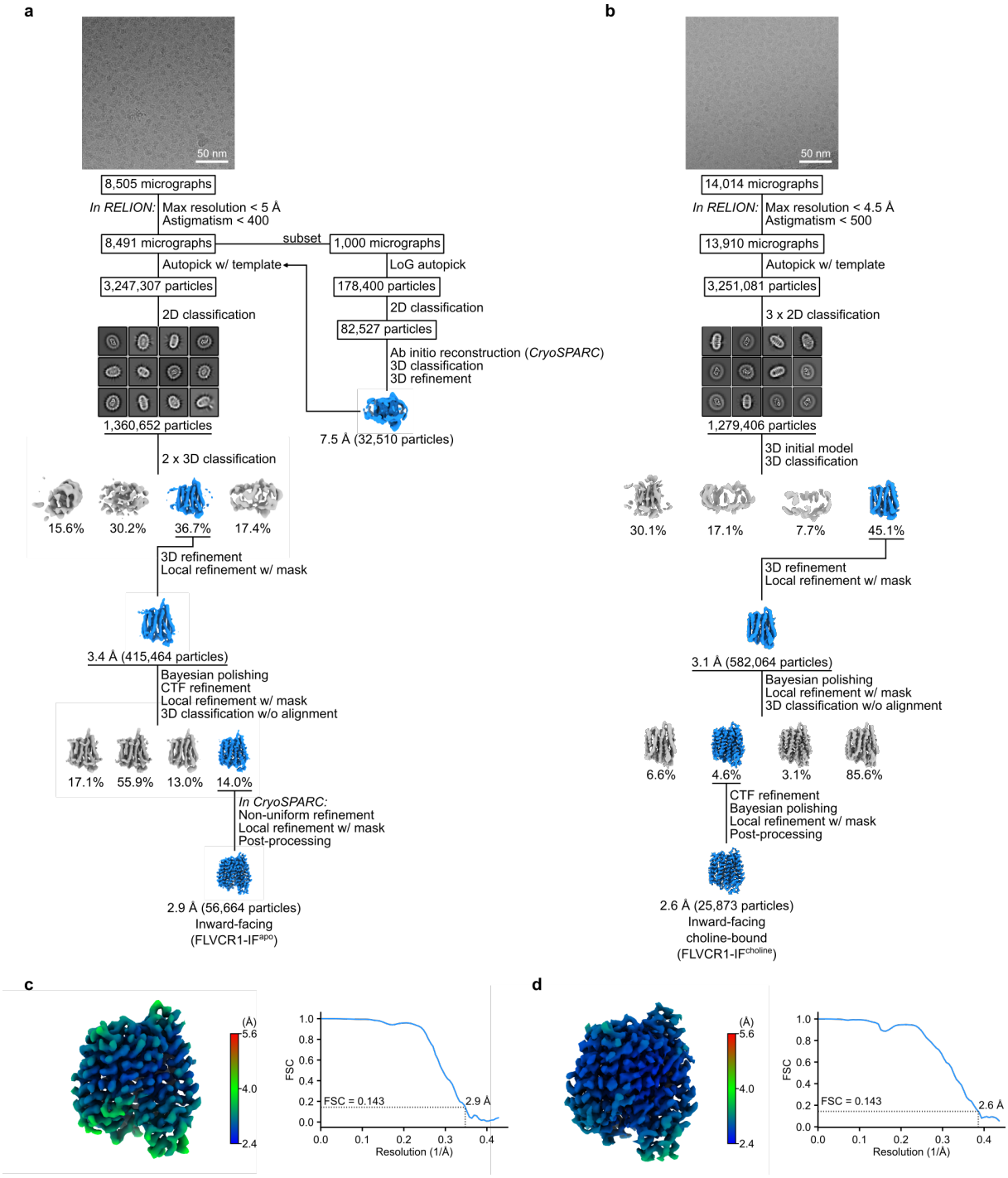

Extended Data Fig. 1: Single-particle cryo-EM analysis of human FLVCR1.

a,**b**, Summary of the data processing procedure of the as-isolated FLVCR1 sample and FLVCR1 supplemented with choline. **c**,**d**, Local resolution estimation (left) and Fourier shell correlation (FSC) curves (right) of the final cryo-EM maps of FLVCR1-IF^{apo} and -IF^{choline}.

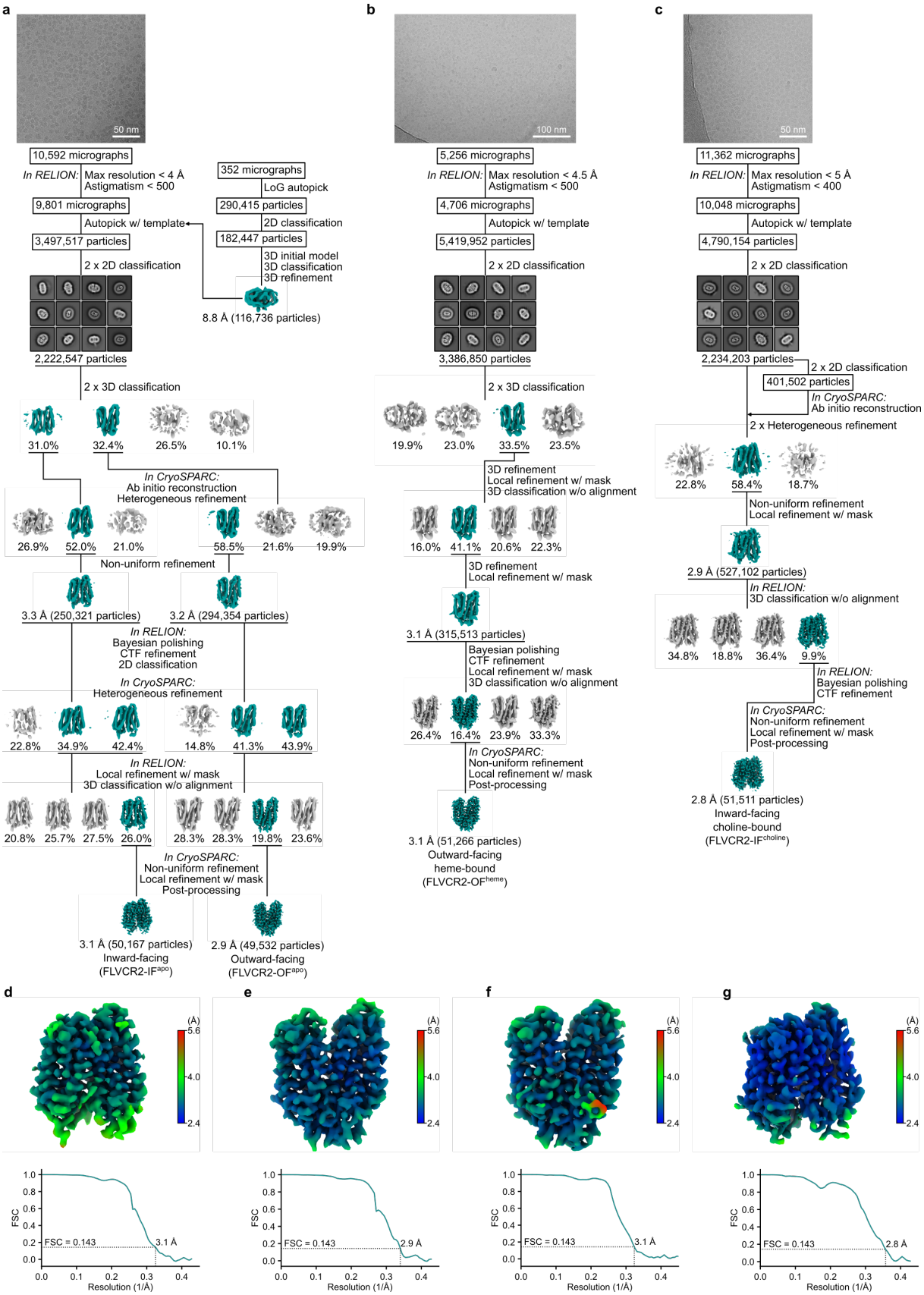

855

856 **Extended Data Fig. 2: Single-particle cryo-EM analysis of human FLVCR1.**

857 **a**-**c**, Summary of the data processing procedure of the as-isolated FLVCR2, heme-supplemented, and

858 choline-supplemented FLVCR2 samples. **d**-**g**, Local resolution estimation (top) and FSC curves (bottom)

859 of the final cryo-EM maps of FLVCR2-IF^{apo}, FLVCR2-OF^{apo}, FLVCR2-OF^{heme}, and FLVCR2-IF^{choline}.

860

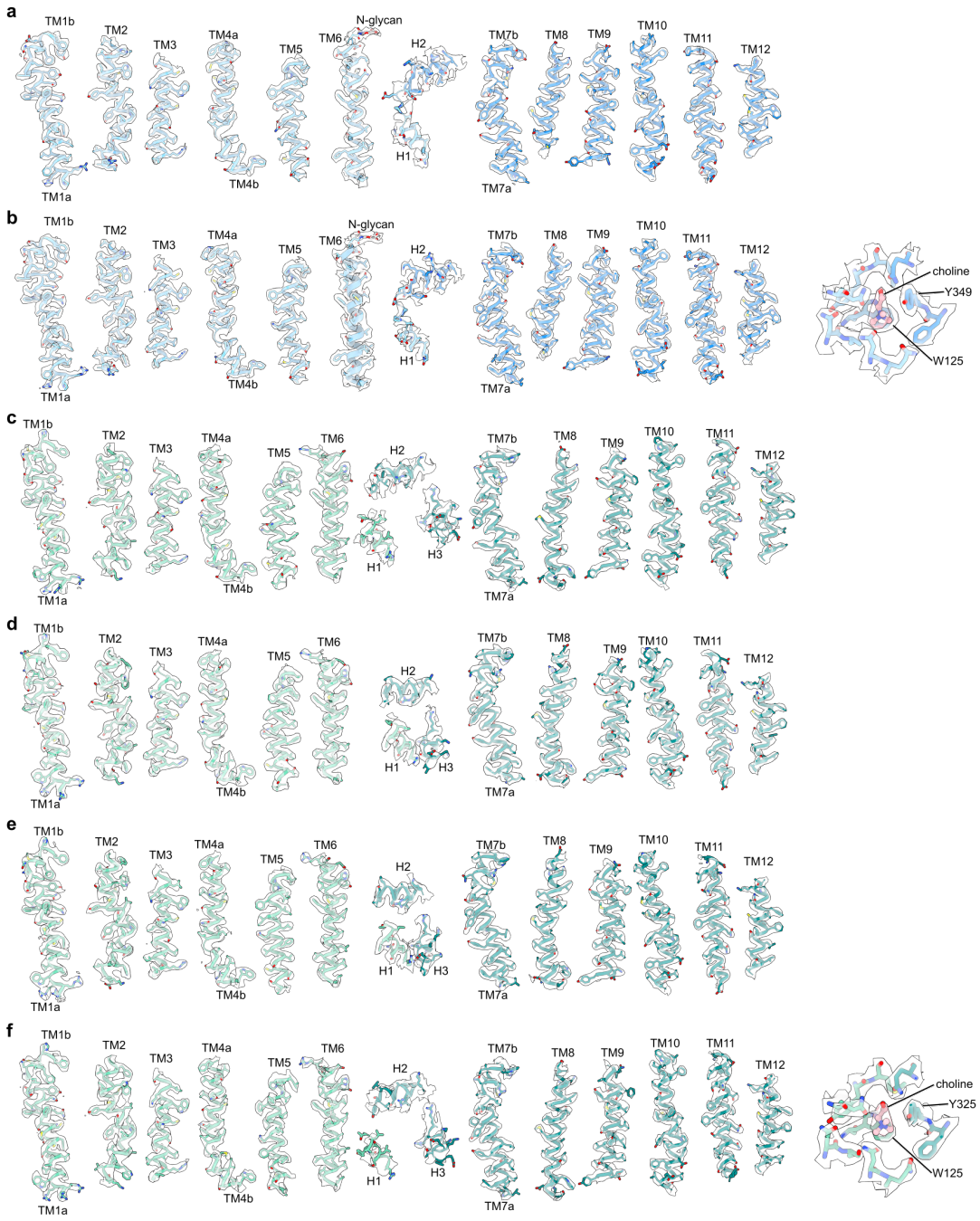

Extended Data Fig. 3: Cryo-EM density and model fitting.

Cryo-EM map and model fits of the transmembrane and intracellular helices of FLVCR1-IF^{apo} (**a**), FLVCR1-IF^{choline} (**b**), FLVCR2-IF^{apo} (**c**), FLVCR2-OF^{apo} (**d**), FLVCR2-OF^{heme} (**e**), and FLVCR2-IF^{choline} (**f**). The map for choline and the surrounding residues is shown for the choline-bound states of FLVCR1 and FLVCR2, respectively.

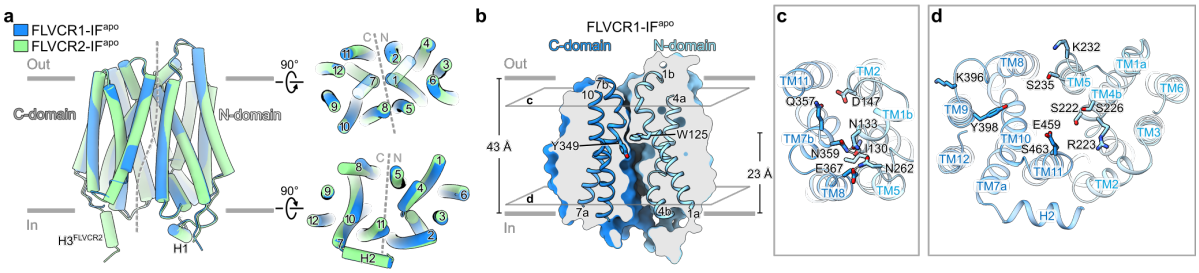

Extended Data Fig. 4: Structural comparison between FLVCR1-IF^{apo} and FLVCR2-IF^{apo}.

a, Structural comparison of FLVCR1-IF^{apo} and FLVCR2-IF^{apo} in tube representation, viewed from the lipid bilayer (left), extracellular side (top-right), and intracellular side (bottom-right). **b**, Cut-away view of FLVCR1-IF^{apo} in surface representation showing the cytoplasmic cavity. Two central aromatic residues are shown as sticks. **c**,**d**, Cross-sections of inter-domain interactions in FLVCR1-IF^{apo} as indicated in (**b**), viewed from the extracellular side (**c**), or from the intracellular side (**d**). Residues corresponding to the inter-domain interaction residues in FLVCR2 are shown.

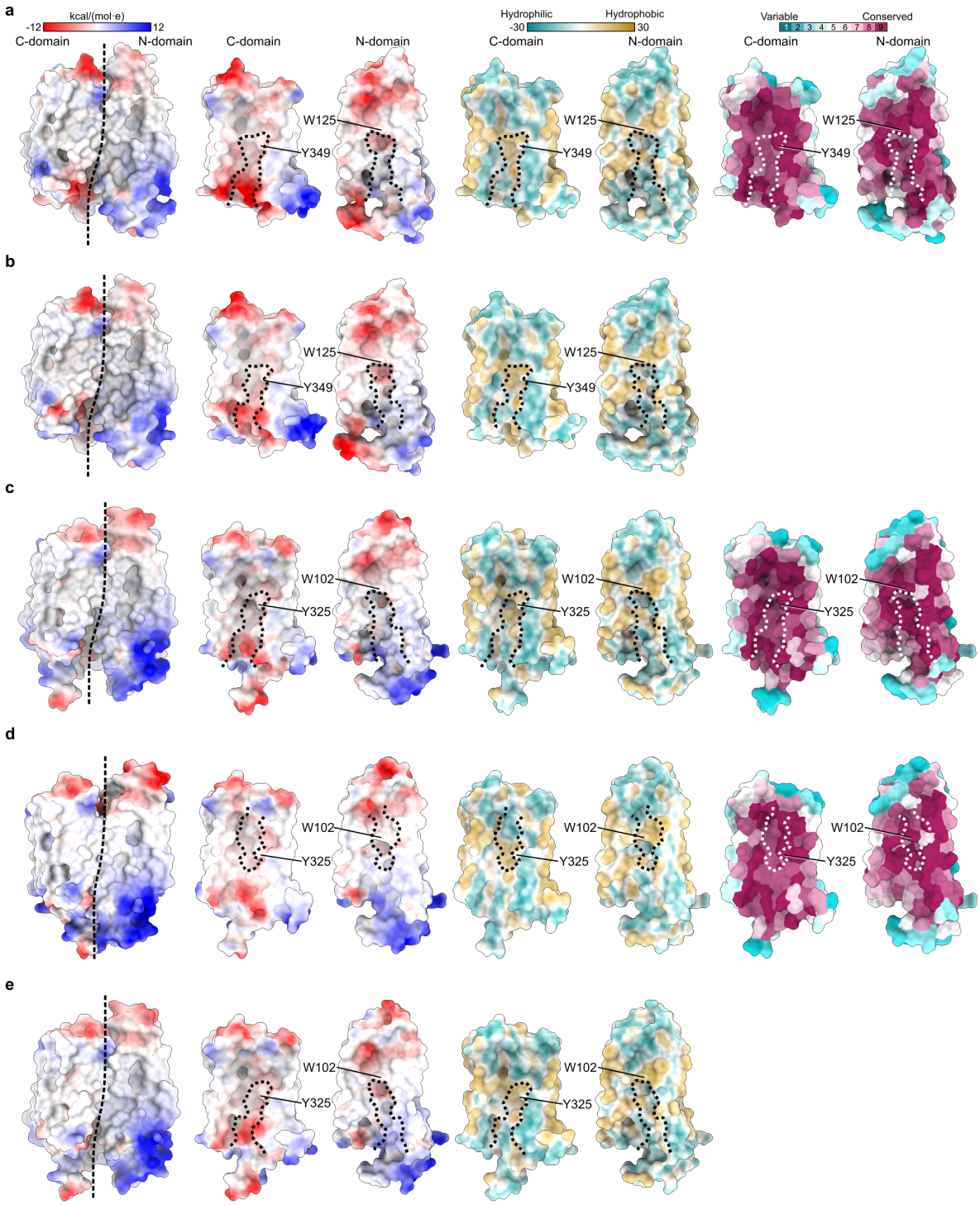

877

878 **Extended Data Fig. 5: Chemicophysical properties of FLVCR structures and conservation analyses.**

879 Surface charge, hydrophobicity, and conservation analyses of FLVCR1-IF^{apo} (**a**), FLVCR1-IF^{choline} (**b**),

880 FLVCR2-IF^{apo} (**c**), FLVCR2-OF^{apo} (**d**), and FLVCR2-IF^{choline} (**e**). From left to right: Surface viewed from the

881 lipid bilayer and both C and N domains viewed from the domain interface coloured by electrostatic

882 potential, the domain interface coloured by hydrophobicity, and the domain interface coloured by

883 sequence conservation. The cavity in the different states of both FLVCRs is outlined with dashed lines.

884 Two important central pocket residues (W125 and Y349 in FLVCR1; W102 and Y325 in FLVCR2) are

885 indicated.

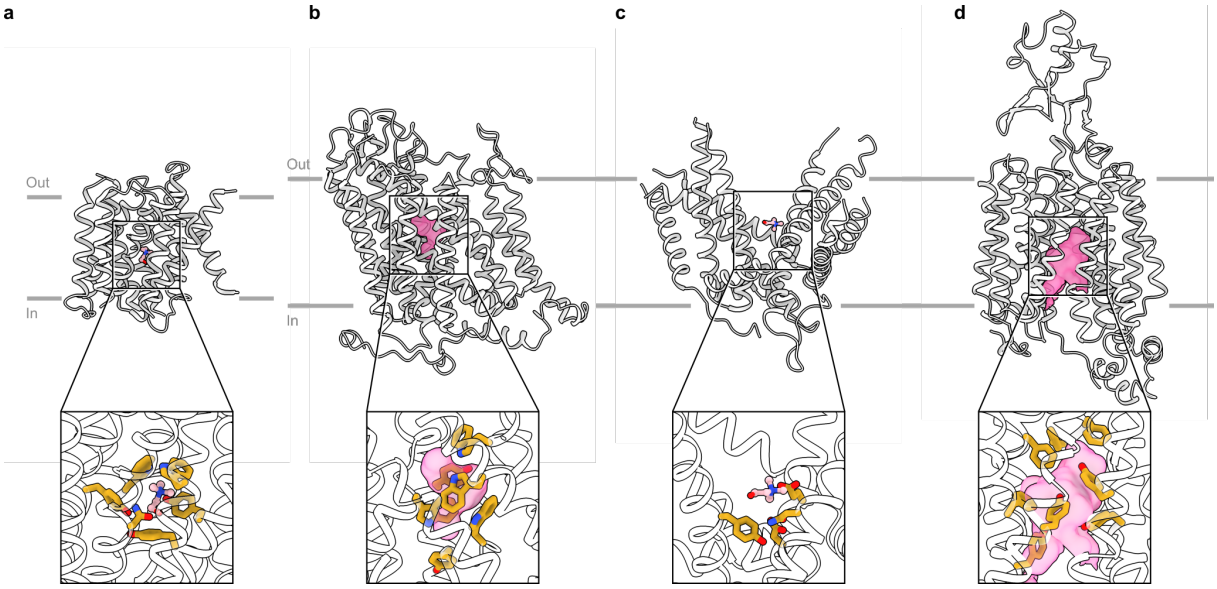

Extended Data Fig. 6: Structures of bacterial and mammalian choline transporters. Experimental or predicted structures of bacterial choline transporter LicB (PDB 7B0K; **a**) and other known human choline transporters SLC5A7 (AlphaFold AF-Q9GZV3-F1; **b**), SLC44A1 (PDB 7WWB; **c**), and SLC22A5 (AlphaFold AF-O76082-F1; **d**). The lower panels show the close-up views of their respective binding sites. Choline or putative choline-binding cavities are highlighted in pink. Choline-binding residues or residues lining a putative choline-binding site are indicated in yellow.

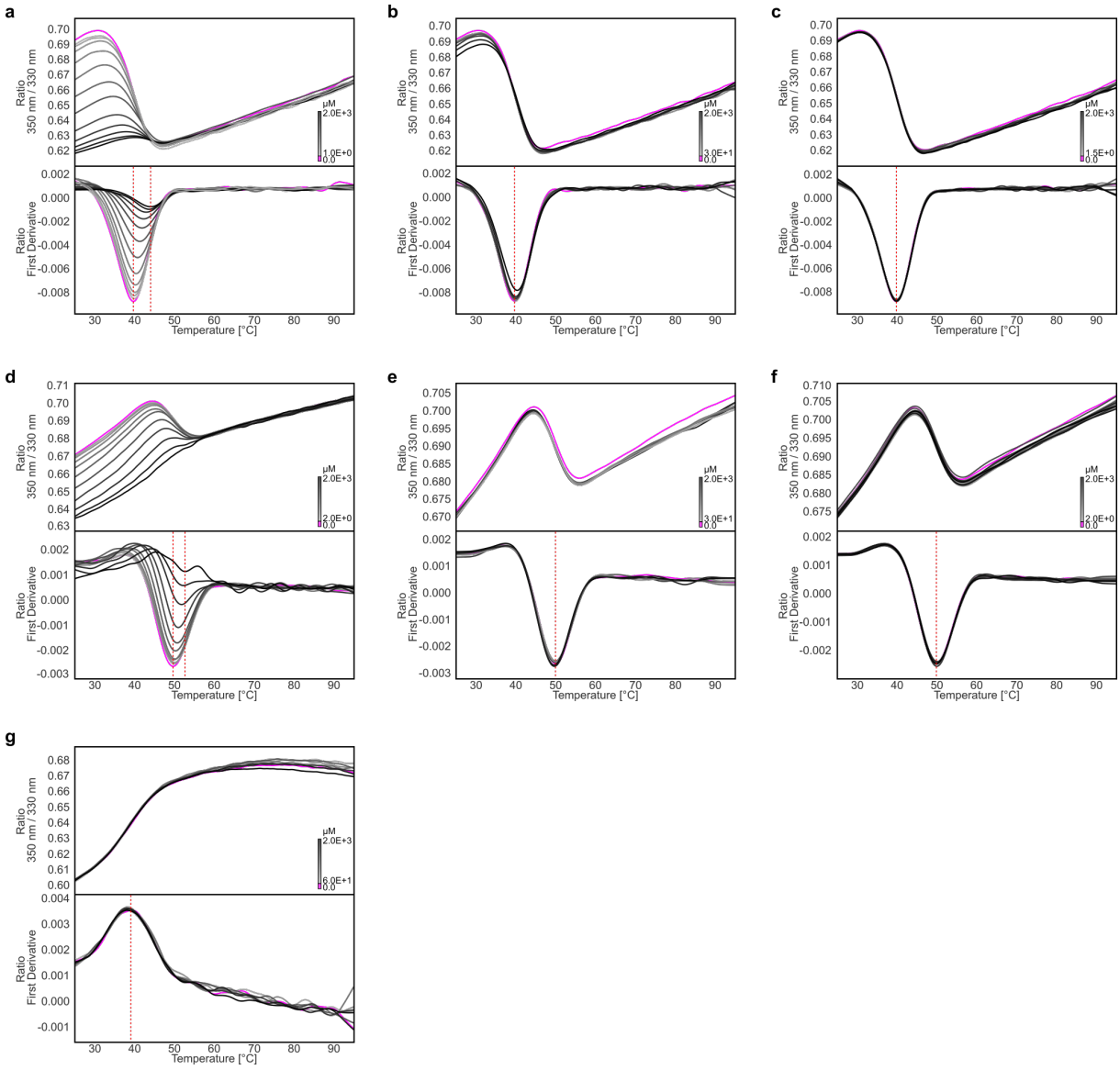

894

895 **Extended Data Fig. 7: Binding affinity screening of FLVCRs in the presence of choline or its metabolites**

896 **by nano differential scanning fluorimetry (nanoDSF).**

897 **a**-**c**, Representative nanoDSF measurements (F_{350}/F_{330}) along a temperature ramp from 25°C to 95°C

898 (top) and the respective first derivative (bottom) of detergent-solubilized FLVCR1 and FLVCR2 in the

899 presence of a serial dilution of choline (**a,d**), phosphocholine (**b,e**), or betaine (**c,f**). **g**, Representative

900 negative-control assay using a purified human sodium transporter from the SLC9 family in the presence

901 of a serial dilution of choline. Magenta lines represent measurements of the samples without choline.

902 Red vertical dashed lines represent the melting temperatures of the samples without choline and the

903 samples of FLVCRs with 2 mM choline.

904

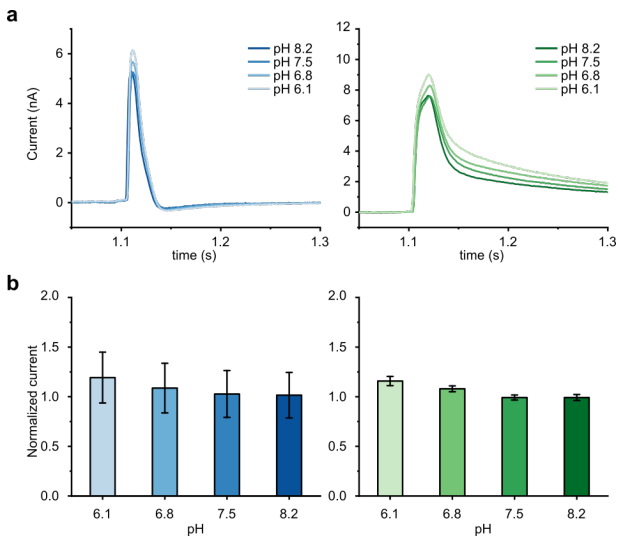

905

906 **Extended Data Fig. 8: SSM-based electrophysiological profiles of FLVCRs in proteoliposomes.**

907 **a**, Current traces for FLVCR1 (left) or FLVCR2 (right) proteoliposomes with buffers at different pH as

908 indicated in the figure. **b**, Normalized peak currents for FLVCR1 (left) and FLVCR2 (right) based on the

909 measurement in (**a**). Data are represented as mean ± s.d. (n = 4).

910

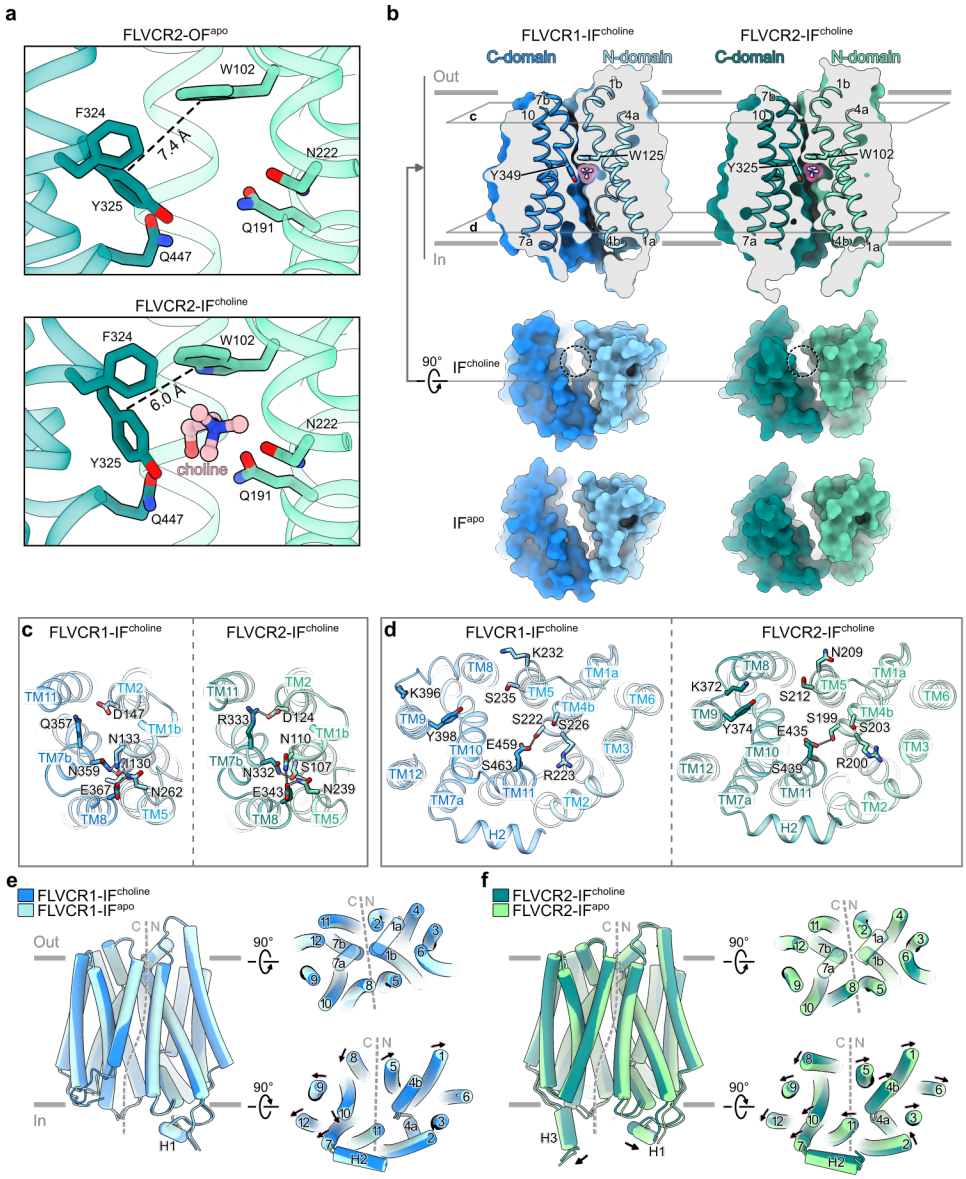

Extended Data Fig. 9: Structural comparison of FLVCRs in their choline-bound inward-facing states. **a**, Choline-binding sites of FLVCR2-OF^{apo} (top) and FLVCR2-IF^{choline} (bottom) with the distance between W102 and Y325 shown as dashed lines. **b**, Cut-away views of FLVCR1-IF^{choline} (top-left) and FLVCR2-IF^{choline} (top-right) showing the inward-facing cavity. Two central aromatic residues are shown as sticks. The surfaces shown below are the IF^{apo} and IF^{choline} states of FLVCR1 (left) and FLVCR2 (right) viewed from the internal side. The dashed circles indicate the peripheral channel in the choline-bound state. **c**,**d**, Cross-sections of inter-domain interactions in FLVCR1-IF^{choline} (left) and FLVCR2-IF^{choline} (right) as indicated in (**b**), viewed from the external side (**c**), or from the internal side (**d**). **e**, Structural comparison

920 of FLVCR1-IF^{choline} and FLVCR1-IF^{apo}, viewed from the lipid bilayer (left), external side (top-right), and

921 internal side (bottom-right). **h**, Structural comparison of FLVCR2-IF^{choline} and FLVCR2-IF^{apo}, viewed from

922 the lipid bilayer (left), external side (top-right), and internal side (bottom-right).

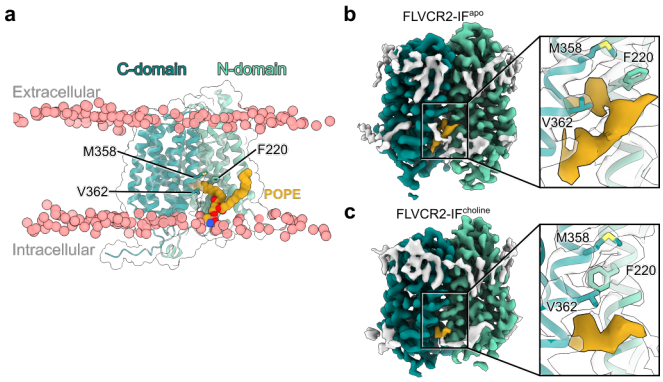

Extended Data Fig. 10: Lateral gate in the inward-facing state of FLVCR2.

a, An MD-snapshot of FLVCR2 in the inward-facing state showing the entry of a lipid acyl group into the lateral gate in the cytoplasmic leaflet. The POPE molecule is shown in yellow and heteroatom colour codes. For simplicity, only the phosphates of the other POPE/POPG are shown as red spheres. **b**,**c**, Cryo-EM density maps of FLVCR-IF^{apo} and -IF^{choline} in viewing angle of the lipid-binding site. The lipid/detergent density is coloured grey. Lipid/detergent density entering the lateral gate is shown in yellow. The three residues at the lateral gate are shown as stick models.